

# Operational experience, improvements, and performance of the CDF Run II silicon vertex detector

T. Aaltonen<sup>p</sup>, S. Behari<sup>q,1,\*</sup>, A. Boveia<sup>h,f</sup>, B. Brau<sup>h,v</sup>, G. Bolla<sup>ae</sup>,  
 D. Bortoletto<sup>ae</sup>, C. Calancha<sup>u</sup>, S. Carron<sup>1,ai</sup>, S. Cihangir<sup>l</sup>, M. Corbo<sup>ab</sup>,  
 D. Clark<sup>c</sup>, B. Di Ruzza<sup>1,d</sup>, R. Eusebi<sup>1,aj</sup>, J. P. Fernandez<sup>u</sup>, J. C. Freeman<sup>l</sup>,  
 J. E. Garcia<sup>ac,n</sup>, M. Garcia-Sciveres<sup>s</sup>, D. Glenzinski<sup>l</sup>, O. González<sup>u</sup>,  
 S. Grinstein<sup>o,b</sup>, M. Hartz<sup>ad,ak</sup>, M. Herndon<sup>q,am</sup>, C. Hill<sup>h,z</sup>, A. Hocker<sup>l</sup>,  
 U. Husemann<sup>af,ao,r</sup>, J. Incandela<sup>h</sup>, C. Issever<sup>h,aa</sup>, S. Jindariani<sup>l</sup>, T. R. Junk<sup>l</sup>,  
 K. Knoepfel<sup>l</sup>, J. D. Lewis<sup>l</sup>, R. S. Lu<sup>a,t</sup>, R. Martínez-Ballarín<sup>u</sup>, M. Mathis<sup>q,an</sup>,  
 M. Mattson<sup>al</sup>, P. Merkel<sup>1,ae</sup>, L. Miller<sup>o</sup>, A. Mitra<sup>a</sup>, M. N. Mondragon<sup>l</sup>,  
 R. Moore<sup>1,w</sup>, J. R. Mumford<sup>q</sup>, S. Nahn<sup>ao,x</sup>, J. Nielsen<sup>s,i</sup>, T. K. Nelson<sup>ai</sup>,  
 V. Pavlicek<sup>l</sup>, J. Pursley<sup>q,y</sup>, I. Redondo<sup>u</sup>, R. Roser<sup>l</sup>, K. Schultz<sup>l</sup>, J. Slaughter<sup>l</sup>,  
 J. Spalding<sup>l</sup>, M. Stancari<sup>l</sup>, M. Stanitzki<sup>ao,j</sup>, D. Stuart<sup>h</sup>, A. Sukhanov<sup>m,1</sup>,  
 R. Tesarek<sup>l</sup>, K. Treptow<sup>l</sup>, R. Wallny<sup>g,k</sup>, P. Wilson<sup>l</sup>, S. Worm<sup>ag,ah,e</sup>

<sup>a</sup>Academia Sinica, Taipei, Taiwan 11529, Republic of China

<sup>b</sup>Institut de Física d'Altes Energies, ICREA, Universitat Autònoma de Barcelona, E-08193, Bellaterra (Barcelona), Spain

<sup>c</sup>Brandeis University, Waltham, MA 02453, United States

<sup>d</sup>Physics Department, Brookhaven National Laboratory, Upton, NY 11973, United States  
<sup>e</sup>CERN, CH-1211 Geneva, Switzerland

<sup>f</sup>Enrico Fermi Institute, University of Chicago, Chicago, IL 60637, United States

<sup>g</sup>University of California, Los Angeles, CA 90095, United States

<sup>h</sup>University of California, Santa Barbara, CA 93106, United States

<sup>i</sup>Santa Cruz Institute for Particle Physics, University of California, Santa Cruz, CA 95064, United States

<sup>j</sup>DESY, Notkestr. 85, D-22603 Hamburg and Platanenallee 6, D-15738 Zeuthen, Germany

<sup>k</sup>ETH Institute for Particle Physics, Schafmattstrasse 20, 8093 Zurich, Switzerland

<sup>l</sup>Fermi National Accelerator Laboratory, Batavia, IL 60510, United States

<sup>m</sup>University of Florida, Gainesville, FL 32611, United States

<sup>n</sup>University of Geneva, CH-1211 Geneva 4, Switzerland

<sup>o</sup>Harvard University, Cambridge, MA 02138, United States

<sup>p</sup>University of Helsinki and Helsinki Institute of Physics, FIN-00014, Helsinki, Finland

<sup>q</sup>The Johns Hopkins University, Baltimore, MD 21218, United States

<sup>r</sup>Institut für Experimentelle Kernphysik, Karlsruhe Institute of Technology, D-76131 Karlsruhe, Germany

<sup>s</sup>Ernest Orlando Lawrence Berkeley National Laboratory, Berkeley, CA 94720, United States

<sup>t</sup>National Taiwan University (NTU), Taipei, Taiwan, Republic of China

<sup>u</sup>Centro de Investigaciones Energeticas Medioambientales y Tecnológicas, E-28040 Madrid, Spain

<sup>v</sup>Department of Physics, University of Massachusetts, Amherst, MA, United States

<sup>w</sup>Massachusetts General Hospital, Harvard Medical School, Boston, MA 02114, United States

<sup>x</sup>Massachusetts Institute of Technology, Cambridge, MA 02139, United States

<sup>y</sup>Brigham and Women's Hospital, Harvard Medical School, Boston, MA 02115, United States

---

☆FERMILAB-PUB-13-015-E

\*Corresponding author

Email address: behari@fnal.gov (S. Behari)

<sup>z</sup>The Ohio State University, Columbus, OH 43210, United States  
<sup>aa</sup>University of Oxford, Oxford OX1 3RH, United Kingdom  
<sup>ab</sup>LPNHE, Universite Pierre et Marie Curie/IN2P3-CNRS, UMR7585, Paris, F-75252  
France  
<sup>ac</sup>Istituto Nazionale di Fisica Nucleare Pisa, Universities of Pisa, Siena and Scuola Normale  
Superiore, I-56127 Pisa, Italy  
<sup>ad</sup>University of Pittsburgh, Pittsburgh, PA 15260, United States  
<sup>ae</sup>Purdue University, West Lafayette, IN 47907, United States  
<sup>af</sup>University of Rochester, Rochester, NY 14627, United States  
<sup>ag</sup>Rutgers University, Piscataway, NJ 08855, United States  
<sup>ah</sup>Rutherford Appleton Laboratory, Science and Technology Facilities Council, Harwell  
Science and Innovation Campus, Didcot OX11 0QX, United Kingdom  
<sup>ai</sup>SLAC National Accelerator Laboratory, Menlo Park, CA 94025, United States  
<sup>aj</sup>Texas A&M University, College Station, TX 77843, United States  
<sup>ak</sup>University of Toronto, Toronto, Ontario M5S 1A7, Canada  
<sup>al</sup>Wayne State University, Detroit, MI 48202, United States  
<sup>am</sup>University of Wisconsin, Madison, WI 53706, United States  
<sup>an</sup>College of William & Mary, Williamsburg, VA 23187, United States  
<sup>ao</sup>Yale University, New Haven, CT 06520, United States

---

## Abstract

The Collider Detector at Fermilab (CDF) pursues a broad physics program at Fermilab's Tevatron collider. Between Run II commissioning in early 2001 and the end of operations in September 2011, the Tevatron delivered  $12 \text{ fb}^{-1}$  of integrated luminosity of  $p\bar{p}$  collisions at  $\sqrt{s} = 1.96 \text{ TeV}$ . The physics at CDF includes precise measurements of the masses of the top quark and  $W$  boson, measurement of CP violation and  $B_s$  mixing, and searches for Higgs bosons and new physics signatures, all of which require heavy flavor tagging with large charged particle tracking acceptance. To realize these goals, in 2001 CDF installed eight layers of silicon microstrip detectors around its interaction region. These detectors were designed for 2–5 years of operation, radiation doses up to 2 Mrad (0.02 Gy), and were expected to be replaced in 2004. The sensors were not replaced, and the Tevatron run was extended for several years beyond its design, exposing the sensors and electronics to much higher radiation doses than anticipated. In this paper we describe the operational challenges encountered over the past 10 years of running the CDF silicon detectors, the preventive measures undertaken, and the improvements made along the way to ensure their optimal performance for collecting high quality physics data. In addition, we describe the quantities and methods used to monitor radiation damage in the sensors for optimal performance and summarize the detector performance quantities important to CDF's physics program, including vertex resolution, heavy flavor tagging, and silicon vertex trigger performance.

*Keywords:* Silicon, Vertex detector, CDF, Tevatron Run II, Detector operations

---

## 1. Introduction

The Tevatron collider at the Fermi National Accelerator Laboratory (FNAL) collided proton and antiproton beams at a center-of-mass energy of 1.96 TeV. The collisions occurred at two interaction points where multipurpose detectors Collider Detector at Fermilab (CDF II) and D0, were positioned.

The CDF II detector [1] was a general purpose detector with cylindrical geometry. The innermost part of the detector consisted of charged-particle tracking detectors, shown in Figs. 1 and 2, which were located inside a superconducting solenoidal magnet which provided a highly uniform 1.4 T magnetic field oriented parallel to the beam axis. Calorimeters and muon systems outside the solenoid provided lepton identification and momentum measurement as well as jet energy measurements. The tracking detectors and calorimeters were used for jet reconstruction, where the former provided identification of jets from heavy (charm and bottom) quarks.

The inner component of the tracking system was a series of silicon microstrip detectors that constituted the CDF silicon detector. Beyond the silicon detector lay the Central Outer Tracker (COT), an open-cell drift chamber. Together with the additional constraints coming from the position of the primary vertex, the COT and Silicon Detector provided resolution on the track momentum transverse to the beam direction,  $p_T$ , of  $\sigma(p_T)/p_T = 0.15\% \cdot p_T/(\text{GeV}/c)$ .

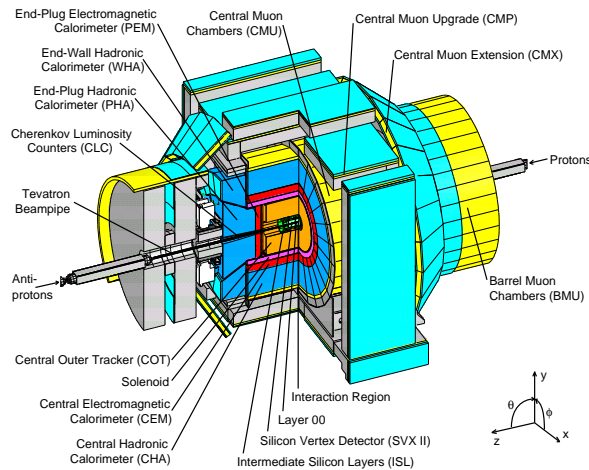


Figure 1: Isometric view of the entire CDF II detector.

CDF II used a cylindrical coordinate system with the  $z$  axis oriented along the proton beam direction and azimuthal angle  $\phi$  measured around the beam axis. The polar angle  $\theta$  was measured with respect to the positive  $z$  (proton-beam) direction and was used to define the pseudorapidity  $\eta \equiv -\ln(\tan(\theta/2))$ .

The physics program of Run II at the Tevatron includes precision measurements of the mass of the top quark and  $W$  boson; bottom and charm physics, including the determination of the  $B_s$  and  $D^0$  mixing parameters; studies of the

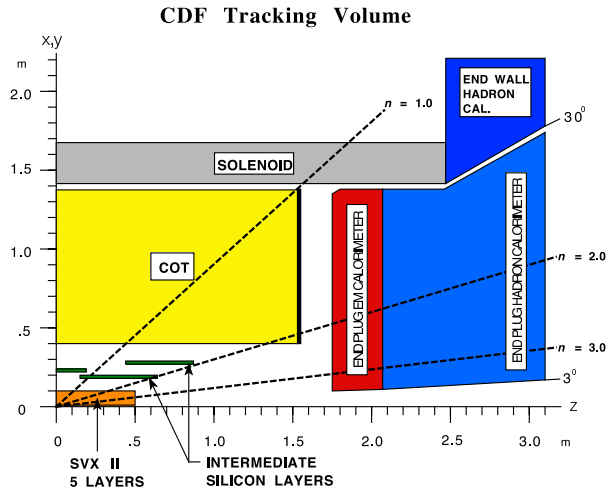


Figure 2: Schematic layout of the CDF II tracking system.

strong interaction (jet multiplicities, diffractive physics, etc.); and searches for objects and phenomena as varied as the Higgs boson, supersymmetric particles, hidden space-time dimensions, and quark substructure [2–5]. All these measurements benefit from a high-resolution tracking detector and many rely heavily on the efficient identification of heavy quarks by detection of displaced secondary vertices, and are enhanced by the capability to trigger on tracks originating away from the beam.

The CDF silicon detector was designed to withstand radiation doses up to 2 MRad (0.02 Gy), the dose expected during the first 2–5 years of CDF operations, with replacement of inner layers planned in 2004 [6]. However, the upgrade project was canceled in 2003, and Run II was later extended into late 2011, with total delivered integrated luminosity of  $12 \text{ fb}^{-1}$ . Several preventive measures were taken to keep the original silicon detector operational and maintain its performance. The most important of these was the decrease in the operating temperature of the detector, which reduced the impact of chronic radiation exposure (Section 5). Steps were also taken to minimize thermal cycles, damage from resonances of wire bonds (Section 3.6), and instabilities and sudden loss of the Tevatron beams (Section 6).

Issues arising from radiation damage of the sensors, aging infrastructure, and electronics were addressed continuously in addition to the basic challenges posed by the inaccessibility of the detector volume and large number of readout channels (approximately 722,000). The operational challenges, improvements to, and the performance of the CDF silicon detector are presented in this paper. Similar experiences with their silicon detectors have been reported by the D0 collaboration [7–9].

This paper is organized as follows: Section 2 provides a general description of the detector, Section 3 gives an overview of the data acquisition, the trigger,

and the interface between them, Section 4 describes the power supplies and the operational experience with them and response to their failures, Section 5 details the design, history, and response to failures in the cooling system, Section 6 gives a review of particle beam incidents, and response to them. Section 7 details the readout calibration, Section 8 is dedicated to the routine monitoring and operations support systems, Section 9 describes the response of the CDF silicon detector to accumulated radiation doses, Section 10 details the performance of the silicon detector and the displaced vertex trigger, and Section 11 gives a summary. As well as new results, this paper compiles final results on material dispersed in several conference proceedings produced over the years by the members of operations team [10–15].

## 2. Detector description

The CDF silicon detector system consisted of three sub-detectors, all with barrel geometry: Layer 00 (L00) [11, 16], the Silicon Vertex detector (SVX-II) [17, 18] and the Intermediate Silicon Layers (ISL) [19]. Unless otherwise stated, detector refers to the CDF silicon detector. The design of the system was driven by the goal of providing excellent spatial resolution in the measurement of charged-particle tracks. These measurements were crucial for the reconstruction of the displaced secondary vertices and therefore, identification of events with bottom-quarks. Figs. 3 and 4 present the schematic layout of the CDF silicon detector, and Table 1 summarizes some of the basic parameters. The design had eight silicon layers to provide tracking which is robust against failure or degradation of individual components.

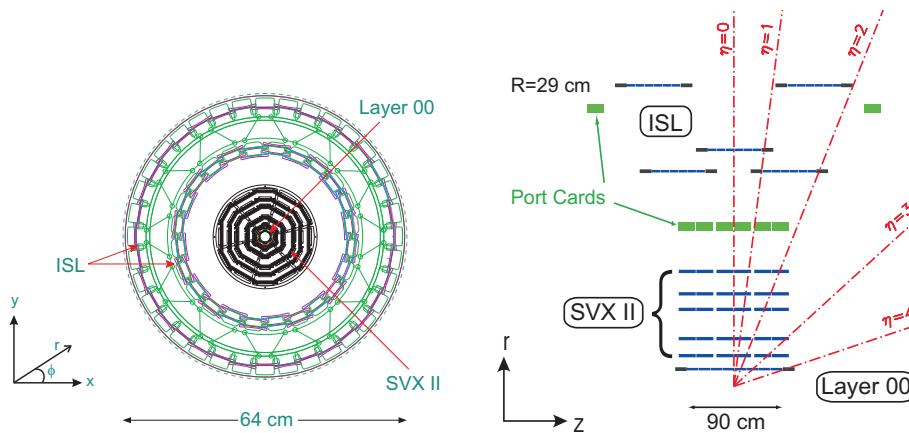


Figure 3: Schematic layout of the CDF silicon detectors showing  $x$ - $y$  ( $r$ - $\phi$ , left) and  $y$ - $z$  ( $r$ - $z$ , right) views. Note that the  $z$  axis is compressed for illustration purposes.

The basic structural unit of a sub-detector was a *ladder*, which consisted of several silicon microstrip sensors bonded in series (3 sensors for L00 ladders, four in SVX-II ladders and six in ISL ladders). Strip width and multiplicity

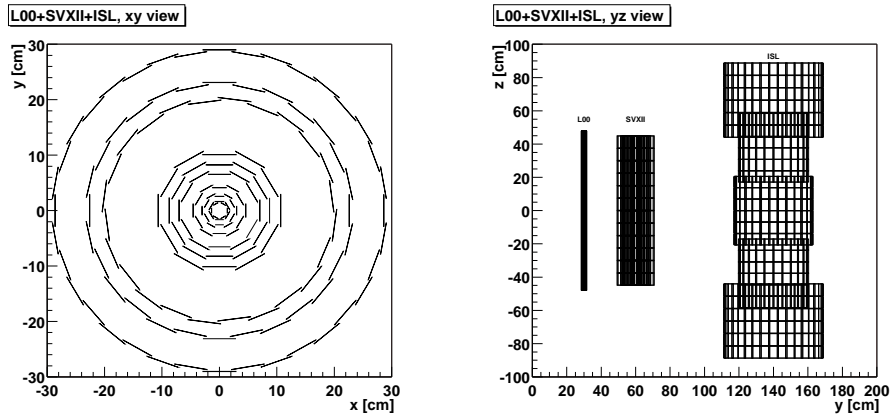


Figure 4: Dimensions, in cm, of the CDF silicon detector system. Shown are  $x$ - $y$  and  $y$ - $z$  views. In the  $y$ - $z$  view, each square corresponds to one sensor and each subdetector has been displaced along the  $y$ -axis for illustration purposes.

depended on the *layer*, or distance from the beam pipe. The sensors were made from high-resistivity n-type silicon with a nominal thickness of  $300\ \mu\text{m}$ . Sensors in L00 were single-sided, providing  $r$ - $\phi$  information, while sensors in the other layers were double-sided, providing both  $r$ - $\phi$  and  $r$ - $z$  information. The sensors in SVX-II layers 0, 1, and 3 used double-metal readout for a  $90^\circ$  strips on the  $r$ - $z$  side. The other double-sided layers used small-angle stereo strips.

The readout was carried out through aluminum strips AC coupled to the implant strips, which are of p-type for the  $r$ - $\phi$  and n-type for the  $r$ - $z$  or small-angle stereo side. A full ladder was read out from both ends through SVX3D readout chips (described in Section 3.3.1) mounted on electrical hybrids. These hybrids were located outside (for L00) or inside (for SVX-II and ISL ladders) of the tracking volume. A circuit board called the *portcard* was located at the periphery of each support structure or bulkhead and formed an interface with the hybrids and readout chips with the rest of the data acquisition system (Section 3).

Layer 00 was a single-sided silicon microstrip detector whose sensors could be biased to higher voltages than the double-sided sensors. It was mounted on a carbon fiber support structure which was in turn mounted directly on the beam pipe, and had an inner radius of 1.15 cm and outer radius of 2.1 cm. Its main purpose was to improve the track impact parameter resolution which was otherwise limited by multiple scattering in the additional material of the SVX-II readout and cooling infrastructure; a secondary purpose was to prolong CDF silicon detector lifetime by providing a backup to SVX-II layer-0. Layer 00 consisted of one layer and had 72 ladders with 13,000 readout channels in total.

The SVX-II detector was built in three cylindrical barrels each 29 cm long. Each barrel contained five layers of double-sided silicon microstrips placed along

Table 1: Summary of L00, SVX-II and ISL basic parameters.

Name	Radius (cm)	Readout	Manufacturer
L00 (narrow)	1.35	$r-\phi$	SGS Thomson, Micron
L00 (wide)	1.62	$r-\phi$	Hamamatsu
SVX L0	2.54	$r-\phi, r-z$	Hamamatsu
SVX L1	4.12	$r-\phi, r-z$	Hamamatsu
SVX L2	6.52	$r-\phi, +1.2^\circ$	Micron
SVX L3	8.22	$r-\phi, r-z$	Hamamatsu
SVX L4	10.10	$r-\phi, -1.2^\circ$	Micron
ISL L6 Central	22.00	$r-\phi, 1.2^\circ$	Hamamatsu
ISL L6 Fwd/Bwd	20.00	$r-\phi, 1.2^\circ$	Hamamatsu
ISL L7 Fwd/Bwd	28.00	$r-\phi, 1.2^\circ$	Micron

the beam axis, with radial coverage from 2.5 to 10.7 cm. Carbon fiber reinforced Rohacell foam [20] provided support to the ladders, and beryllium bulkheads provided additional support and alignment on each end. Therefore the detector consisted of six bulkheads ( $z$ -segmentation), each with 12 wedges ( $\phi$ -segmentation) consisting of 5 layers ( $r$ -segmentation). In total, it had 360 ladders with 405,504 channels in the system. One side of each microstrip sensor provided tracking information in the  $r-\phi$  plane, with strips oriented parallel to the beam direction, while the other side had strips oriented either perpendicular to the beam axis, providing  $90^\circ$  information, or at an angle of  $\pm 1.2^\circ$  with respect to the beam axis, providing small-angle stereo information. Three of the five SVX-II layers had  $90^\circ$  sensors, while the remaining two layers had small-angle stereo strips, as detailed in Table 1. The readout chips and electric hybrids were mounted on the surface of the SVX-II silicon sensors. SVX-II was read out in a strict  $\phi$ -wedge geometry in order to feed the secondary vertex trigger, described in Section 3.1.1.

The ISL was located between SVX-II and the COT drift chamber. It consisted of one central ( $|\eta| < 1$ ) layer of silicon at a radial position of 22 cm and two forward ( $1 < |\eta| < 2$ ) layers at 20 cm and 28 cm. Mechanical support for the ladders was provided by carbon fiber rings. ISL had 148 double-sided ladders of 55 cm length each with a total of 303,104 channels. An ISL ladder was composed of three microstrip sensors bonded together. Like SVX-II, one side of each sensor provided tracking information in the  $r-\phi$  plane while the other side provided tracking information in the  $r-z$  plane with  $\pm 1.2^\circ$  stereo angle. Also like SVX-II, the readout chip hybrids were mounted on the sensors.

Fig. 5 gives a historical account versus time (left) and integrated luminosity (right) of the fraction of detector ladders included in data taking since start of commissioning in 2001. Aside from variation during the start-up period, stable detector operation is observed over the long term data taking period. The rate of corruption in data transmission out of the detector (referred to as "digital

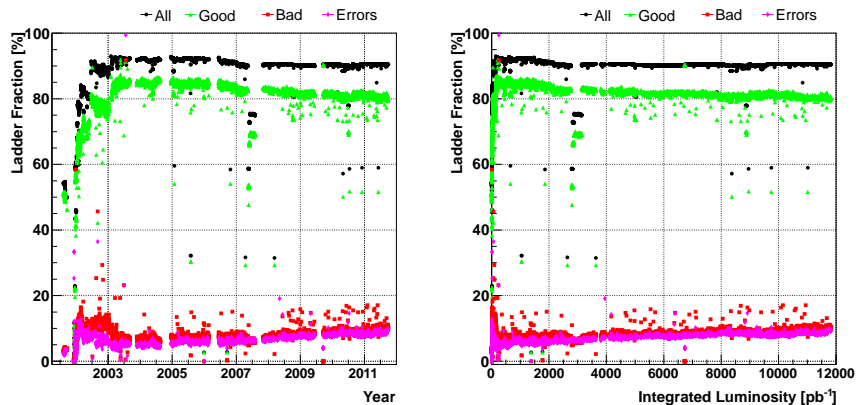


Figure 5: Fraction of ladders which were powered (black circles), considered good (green triangles) and bad (red squares) versus time (left) and versus integrated luminosity (right). A ladder is considered good if it has less than 1% digital errors. Also shown is the average digital error rate (pink diamonds). The actual fraction of good ladders is larger as it does not include ladders whose digital errors are corrected by the offline reconstruction software.

errors”) rises with time. Some of this corruption was recovered with offline processing by using knowledge of the data structure to identify and correct erroneous bits.

### 3. The silicon detector data acquisition system

The data acquisition (DAQ) system of the silicon detector was responsible for reading out and digitizing the charge collected by the 722,432 silicon strips. The DAQ worked in coordination with the CDF trigger system that selected events (proton–antiproton collisions) of interest [1]. The DAQ system was comprised of radiation-hard readout ASICs mounted on the detector, feeding optical data links and a chain of VME boards that coordinated the DAQ process and that collated and processed the data. The unique feature of the DAQ system was the integration of the silicon detector with the secondary vertex trigger (SVT) which had never been attempted at a hadron collider.

The first half of this section (Sections 3.1- 3.4) describes the CDF DAQ and then details the components of the silicon detector DAQ. The second half (Sections 3.5.1- 3.9) describes the commissioning and operations experience, which includes the unexpected behaviors of the SVX3D chip, noise from L00, and effect of radiation on the DAQ.

#### 3.1. CDF timing and trigger

The CDF trigger and DAQ systems were synchronized to the Tevatron beams. The Tevatron divided the proton and antiproton beams into 3 trains, separated by  $1.4 \mu\text{s}$ , and each train was composed of 12 bunches separated by 396 ns. In total there were 36 bunches of protons and antiprotons. It took



21  $\mu\text{s}$  to complete one revolution of the Tevatron. The orbits of the proton and antiproton beams were set to collide every 396 ns<sup>1</sup> at the two points where the CDF and D0 detectors were located.

The CDF clock signals were derived from the Tevatron clock system. The most fundamental clock was derived from the 53 MHz Tevatron radio frequency (RF) system.<sup>2</sup> The Tevatron also sent a signal corresponding to the first proton bunch, with a period of 21  $\mu\text{s}$  (1113 Tevatron RF clock periods) in phase with the RF clock. Further details on the Tevatron beam structure and clocks are available in [21] and references therein. The fundamental CDF clock was derived by dividing the Tevatron RF clock by 7, which gave a period of 132 ns and phased with the first proton bunch clock. Additional clock signals were derived for valid bunch crossings and the gaps between trains.

At a hadron collider, only a small fraction of events are from interesting physics processes. The CDF trigger was responsible for identifying these interesting events in real time. CDF employed a three-level trigger system, where each level used more refined information than the previous level to select events. The first level (L1) ran synchronously with the CDF clock and had a fixed latency of 5.5  $\mu\text{s}$ . It reduced the event rate from 1.7 MHz to less than 35 kHz, and was implemented with custom hardware [1]. When events were selected by L1, the data for non-silicon detectors were stored in one of four buffers, pending processing by the second level (L2). L2 was an asynchronous trigger, comprised of dedicated hardware and software, that selected a subset of the L1 triggered events. It reduced the peak rate of accepted events to  $\sim 800$  Hz. The third level (L3) was a software trigger that ran a fast version of the offline event reconstruction on a computer farm using all data from the CDF detector. It selected a subset of L2 triggered events for permanent storage at a rate of  $\sim 150$  Hz. Overall, the CDF trigger selected  $\sim 1$  in 11,000 collisions for permanent storage.

### 3.1.1. SVT

A unique feature of the CDF's L2 trigger was the ability to select events with a displaced vertex which were characteristic of bottom quark hadron ( $b$ -hadron) decays. This method of selecting hadronic  $b$ -decay events was more efficient than previous leptonic triggers that relied on the rarer semi-leptonic  $b$ -quark decay. This displaced vertex trigger, known as the Silicon Vertex Trigger (SVT), significantly increased CDF's yield of  $b$ -hadrons for analysis.

The SVT used data from the CDF silicon detector and COT to perform precision tracking quickly. Tracks were found by combining information from the COT-based *extremely fast tracker* (XFT) [22] and SVX-II axial layers to patterns stored in look-up tables. The resulting tracks in the  $r$ - $\phi$  plane were used to calculate the 2D distance ( $L_{xy}$ ) of a track pair intersection from the primary vertex. A key development of the SVT hardware was the custom chip-

---

<sup>1</sup>The Tevatron proton-antiproton collision rate was intended to be upgraded to 132 ns, for which the CDF DAQ system was designed, but this change was not implemented.

<sup>2</sup>The central Tevatron RF system fed the Tevatron's accelerating RF cavities.

based pattern recognition (associative memory). CDF was the first detector at a hadron collider to implement a displaced vertex trigger. Further information on the SVT can be found in [23–25] and references therein. The demands of SVT to reconstruct tracks and identify tracks displaced from the interaction point drove the SVX-II design and led to the wedge and barrel layout, the tight construction alignment tolerances, and the SVX-II DAQ design that is discussed in this section.

### *3.2. CDF silicon DAQ architecture*

SVX-II was designed for SVT, which required a specialized DAQ system to provide silicon strip data in 20-40  $\mu$ s. The ISL and L00 that came as extensions to the CDF silicon detector project inherited the SVX-II DAQ. Thus the SVX-II DAQ defined the entire CDF silicon detector DAQ. SVT demanded SVX-II provide data after every L1 accept decision (L1A) by the trigger system. This required deadtimeless readout to guarantee silicon data were always available. Also, to reduce the time to deliver and process the data, only information from silicon strips which collected a significant amount of charge relative to the nominal noise signal was propagated to SVT. Therefore the silicon readout volume, and thus readout time, was driven by the underlying physics processes that drove the occupancy of the detector. It was only by meeting these design challenges that allowed the combination of SVX-II and SVT to be integrated into the CDF trigger.

Fig. 6 shows a schematic diagram of the silicon DAQ system. The process was coordinated by a central controller that interfaced with the trigger system, broadcasted commands to the individual ladders, and controlled data flow through feedback signals from the VME readout buffers. The digitized data from each ladder was transferred in parallel to the allocated readout buffer. The data were buffered until a L2 decision arrived and was either transmitted to L3 or discarded. The Silicon DAQ was synchronized to the CDF clock.

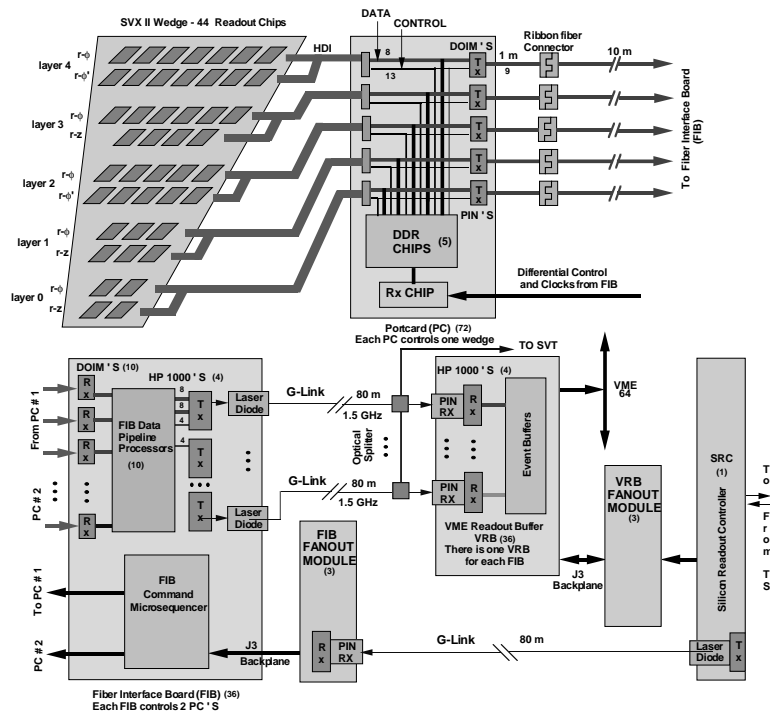


Figure 6: A schematic diagram of the silicon detector DAQ system. The SVX-II wedge and portcard, at the top half of the figure, were known together as the on-detector electronics as they were located directly on the silicon detector. The components, in the lower half of the figure, were known as the off-detector electronics. The FIB and FIB fanout were located in the CDF collision hall. The VRB, VRB fanout and SRC were in the CDF counting room which was located above the CDF collision hall. ISL and L00 DAQ were identical except the SVX-II wedge was substituted with a ISL and L00 wedge, respectively.

The electronics were divided into an on-detector part, mounted directly on the silicon detector, and an off-detector part, located in VME racks in the CDF collision hall and in the CDF counting room (Fig. 6).

### 3.3. On-detector electronics

The on-detector electronics were responsible for acquiring and digitizing the charge from the silicon strips and then transmitting the data to the off-detector electronics. The on-detector electronics consisted of the SVX3D readout chip, the portcard, and DOIM optical data links that are described below.

#### 3.3.1. The SVX3D readout chip

The SVX3D ASIC was responsible for acquiring charge from the silicon strips and digitizing them. It was a custom, radiation-hard, deadtimeless, 128-channel device [26, 27], capable of recording charge simultaneously from all 128 channels every 132 ns and had an 8-bit wide output running at 53 MHz. All 128 channels were digitized simultaneously using an 8-bit grey-coded modified Wilkinson type analog-to-digital converter (ADC) that included event-by-event dynamic pedestal subtraction (DPS). With DPS, which is described later in this section, it was no longer necessary to read out every strip for an offline pedestal subtraction. Therefore the SVX3D could implement data reduction logic (sparsification) to remove channels that were below a set threshold to reduce further the readout time. In this way, the readout time was dictated by the occupancy of the silicon detector. The SVX3D's deadtimeless operation, DPS, and sparsification were essential for SVT.

The SVX3D was manufactured using the Honeywell CMOS 0.8  $\mu\text{m}$  radiation-hard process. From irradiations up to 4 MRad with  $^{60}\text{Co}$  sources and 15 MRad with a 55 MeV proton source, the chip noise in the innermost layer of SVX was expected to increase by 17% after  $8\text{ fb}^{-1}$  (3.1 MRad) [28].

The operations of the chip were divided into an analog front end (FE) and a digital back end (BE). The FE was responsible for acquiring charge from the silicon strips and buffering them into a circular analog pipeline. The BE digitized the charge from the pipeline and any channels above a programmed threshold were sent to a readout FIFO. The FE and BE were driven independently by the CDF clock and Tevatron RF clock, respectively, which allowed the deadtimeless operation.

The chip operation began with an initialization phase which set various operational parameters such as the signal polarity, chip identification number (chip ID), and readout mode. After the initialization phase, the FE changed to the acquisition mode, and the BE alternated between digitization and readout, until a new initialization was performed.

Each FE channel consisted of a charge integrator coupled to a 47 stage circular analog capacitor pipeline; 42 pipeline cells were allocated for the L1 latency, four for L2 buffers, and one reserved to measure the pipeline pedestal. Every CDF clock cycle, the FE charge integrator acquired charge from the silicon strips and transferred it to an empty cell in the analog pipeline. The FE

was reset at every bunch crossing. Whenever a L1 decision to keep an event arrived, the appropriate pipeline cell was marked and skipped over until it was digitized. Under normal operations, up to four pipeline cells could be marked.

A marked analog pipeline cell (capacitor) was digitized by the BE. The voltage across the marked pipeline capacitor, subsequently referred to as the *strip voltage*, went to the input of a comparator. The other input of the comparator was a voltage ramp shared by each channel's comparator. At the start of digitization, the common voltage ramp started and an 8-bit grey-code counter started to increment. A channel's comparator changed state as soon as the voltage ramp was larger than its strip voltage, which triggered a latch to store the current value of the 8-bit counter. Therefore channels with smaller strip voltages would trigger their latches earlier. The common pedestal subtraction was implemented by delaying the counter until the first 33 comparators had changed state. The choice of 33 channels came from a study to optimize pedestal removal with signal efficiency. DPS implicitly assumes a constant chip-wide pedestal<sup>3</sup> and insulates the strip charge measurement from environmental noise.

The SVX3D implemented three modes of data reduction: read out of strips above a set threshold (*sparse*), sparse strips and adjacent below-threshold strips (*nearest neighbor*, *NN*), and no data reduction (*read-all*). Sparse mode had the smallest data volume and therefore smallest readout time but NN was chosen as it allowed addition of neighbor strips below threshold. Additional information provided in the NN mode also proved useful for correcting single bit errors. Except in the read-all mode, the data volume was driven by the underlying physics that drove the occupancy of the silicon strips.

Multiple chips were chained together to read out a single silicon sensor; two for the innermost (narrowest) layer and up to 16 for the outermost (widest) layer. Chip initialization and commands were transferred serially from the first chip in the chain to the last chip in the chain. The first strip of the first chip and last strip of the last chip in the chip chain were always read. Data from each chip in the chip chain were transmitted one-by-one on a common data bus. The data from each chip included the chip ID and the SVX3D channel number of each read strip. There were 5644 SVX3D readout chips in the CDF silicon detector which dissipated approximately 3 kW of power, thus active cooling was essential for stable operations (Section 5).

### 3.3.2. Portcard

The portcard was the interface between the on-detector and off-detector electronics. It relayed SVX3D commands and trigger signals from the DAQ boards and passed on power to bias the silicon sensors and chip chains from the power supplies (Section 4). Data from the chips chains passed through the portcard onto the optical data links (DOIMs) (Section 3.3.3). As the portcards were located within the silicon detector, they were designed to have low mass to

---

<sup>3</sup>This assumption was not true for L00 and DPS was turned off for L00 readout (Section 3.7).

minimize the radiation length, to withstand radiation doses of up to  $\sim 200$  kRad ( $\sim 10 \text{ fb}^{-1}$ ), and with high heat transfer capability [29].

### 3.3.3. *Optical data link: DOIM*

The Dense Optical Interface Module (DOIM) was the optical data link used to transmit data from a chip chain to the off-detector electronics [12]. Each DOIM had a transmitter unit (TX) located on the Portcard and a receiver unit (RX) in an off-detector VME-transition module (Fig. 6). The TX and RX were connected by optical fibers. Each DOIM was capable of transmitting 8-bit wide data at 53 MHz with an error rate of less than 1 in  $10^{12}$  words.

The DOIM TX housed twelve 1550 nm InGaAsP edge emitting lasers in a single package. Only 9 of the 12 were used: 8 to transmit data and one as a data-strobe. The DOIM RX was a InGaAsP/InP PIN diode array. It received the optical signal from the TX and converted it back to an electrical signal. The DOIM TX was tested for radiation hardness with 30 MeV, 63 MeV, and 200 MeV protons with radiation doses up to 2 MRad. The light degradation was measured to be 10% after 200 kRads [30].

### 3.4. *Off-detector electronics*

The off-detector electronics were responsible for coordinating the silicon DAQ process as well as processing and packaging the digitized silicon strip data for the SVT and the CDF DAQ.

The off-detector electronics were housed in eighteen 9U VME crates using VME64 [31]. Of these eighteen crates, eight were located in the CDF collision hall close to the CDF detector, while the other ten were located in a counting room in the CDF assembly building (Fig. 6). The main difference between the two sets crates was the use of two different custom J3 backplanes to accommodate different types of boards. All together, there were 164 VME boards.

Because the data from the SVX3D chip chains were sparsified, the first strip of the first chip and last strip of the last chip of the chip chain were always reported in order to identify the start and end, respectively, of the chip chain data stream. The off-detector electronics appended its own unique header to these data. The combination of the header, chip ID, and SVX3D channel encoded the unique location within the silicon detector of each digitized charge.

#### 3.4.1. *Silicon readout controller (SRC)*

The SRC was the master controller of the silicon detector DAQ and also acted as the interface to the CDF DAQ and trigger systems. The SRC was housed in a rack in the CDF counting room, which was also shared with the VME readout buffers (VRB), and received the clock and the beam structure from the central CDF clock fanout. It communicated with the Trigger Supervisor (TS), which was the central CDF trigger processor. The SRC also provided the central clock to the entire CDF silicon detector, which was kept in sync with the CDF clock using a phase locked loop (PLL). The SRC commands, clock, and trigger signals were transmitted by the SRC via a Transition Module (SRCTM) to the

Fiber Interface Board (FIB) crates in the CDF collision hall using a GLINK [32] optical link running at 53 MHz.

The Silicon DAQ was originally designed to be driven by a single SRC. However, the need to read out all channels of L00 every event (Section 3.7) required two SRCs, one to drive SVX-II and another to drive ISL and L00 (Section 3.7.1). Implementation of the second SRC also helped mitigate the *wirebond resonance* problem (Section 3.6).

#### 3.4.2. Fiber interface board (FIB)

The Fiber Interface boards (FIB) were housed in eight crates located in the four corners of the CDF collision hall. SVX-II and ISL/L00 had four FIB crates each. The signals from the SRC were received by a FIB Fanout (FFO) board in each FIB crate and distributed to the FIBs in its crate via a custom J3 backplane. Each FIB communicated with two portcards via a FIB Transition Module (FTM) on the backside of the FIB crate. It converted the high-level SRC commands into a sequence of instructions suitable for the SVX3D chip chains, which were sent with clock and trigger signals to the two portcards. The FTMs also housed the DOIM RX that received the digitized SVX3D data, which were passed to the FIB. The FIB formatted the data stream, appended its own unique header, and sent the data on four GLINKs to the VME Readout Buffers (VRB) with a copy sent to the SVT through optical splitters.

#### 3.4.3. VME readout buffer (VRB)

The VME Readout Buffers (VRB) were located in the VRB crates in the CDF counting room. Two VRB crates also housed the two SRCs. The VRB buffered the data from the FIBs until a L2 decision was made by the CDF trigger system, upon which the event was moved to the output buffer and was collected by the Event Building system using the VME Bus. The communication between the VRBs and the SRC was handled by the VRB fanout system, which enabled the SRC to manage the buffer provided by the VRBs.

The data from each VRB crate were transferred in parallel to the event builder, which combined segments from the crates into an event record which was then passed to L3. The SVX-II had 6 VRB crates that corresponded to the 6 SVX-II bulkheads. The ISL and L00 originally had two and one VRB crates, respectively. To cope with high instantaneous luminosity (above  $10^{32} \text{ cm}^{-2} \text{ s}^{-1}$ ), it was necessary to reduce the size of the data segments arriving from the VRB crates. In 2006, the ISL and L00 VRB crates were mixed and an additional VRB crate was added (Section 3.7.2).

#### 3.5. DAQ commissioning

Prior to installation, the VME based hardware and onboard detector electronics were thoroughly tested through the use of test stands and data emulation at various levels to verify the functionality and robustness of these systems. However, due to time constraints, there was limited ability to test the two systems together after installation. Together with the unforeseen consequences of

the environment in the collision hall, this led to several problems emerging in the course of the first few years of operation that required immediate attention to alleviate data corruption and potential damage to the detector. The wirebond resonance and L00 noise problems were severe and are described separately in Sections 3.6 and 3.7 respectively. It took from 2001 to 2003 to fully commission the silicon detector.

### 3.5.1. SVX3D commissioning

The SVX3D chip was thoroughly tested during its development. But a number of unexpected behaviors, listed below, were encountered during commissioning. The chip would latch to a state where the chip current increased until it exceeded the power supply safety limit and forced a power supply shut down (trip). These behaviors were circumvented by modifying the SRC, VRB and FIB firmware.

*Abort digitize.* The SVX3D chip had a feature to abort digitization before completion if L2 had already rejected the event. However this feature made the chip enter the high current state and trip. The SRC and FIB firmware were modified to allow the SVX3D chip to always complete digitization which stopped these failures.

*Fifth L1 accept.* The SVX3D chip could accommodate up to four L1A signals without releasing a cell in the analog pipeline (Section 3.3.1). If a fifth L1A arrived before a pipeline cell was released, the chip would transition to either read-all mode or suppress all readout. The SRC firmware kept track of the number of unreleased pipeline cells, and was modified not to send the fifth L1A to the chips, and instead to send an error signal back to the CDF DAQ. This error signal forced a silicon CDF DAQ reset and re-synchronization.

*Keep-alive.* At least every  $270\ \mu\text{s}$ , a command had to be sent to the chip chains to prevent chips from entering the high current state and tripping. The SRC firmware was updated to send these *keep alive* signals every  $270\ \mu\text{s}$  in the absence of any commands. But the SRC state machine was driven by the CDF clock and any glitches or interruptions of this clock would also delay or interrupt the delivery of these keep-alive signals, which would result in large portions of the chips tripping off. Given the sensitivity of the silicon detector to any clock glitches, administrative procedures were implemented requiring permission from either the CDF silicon detector project leader or the head of CDF detector operations before work was done on on the CDF clock or Tevatron clock.

*AVDD2 errors.* There was a class of unrecoverable failures that affected 6% of the SVX3D chips and could be reproduced only by disabling one of SVX3D's analog voltage lines (AVDD2). The observed symptoms were loss of communication with the FE, an increase in the SVX3D's BE current, and loss of communication to chips beyond the affected chip. This class of failure typically occurred after a beam incident (Section 6) or a large temperature change, such



as a cooling system failure. This type of failure became infrequent after 2003 (Figs. 8 and 9) when operation procedures during shutdowns were changed to minimize thermal cycles, coincident with a sharp decline in the frequency and severity of beam incidents.

### 3.5.2. DAQ board enhancements

Commissioning of the silicon detector, the SRC, VRB and FIB firmware were extended to circumvent the unexpected behaviors of the SVX3D readout chip, which are documented in Section 3.5.1. In addition, minor problems appeared when the off-detector and on-detector components of the system were integrated. A few of these issues are described in detail to illustrate the type of problems encountered and solutions implemented.

Data were lost due to failures in the transmission of the clock signal from the FIB/FTM to the portcard. Electronic components on the fiber interface input of the FIB were replaced to increase the tolerance of varying duty cycles on a signal that carried the clock information. The clock rate was known, and failures in the transmission of its signal were overcome by providing an identical backup clock signal. The firmware was also updated to increase the allowed width of the front-end clock from about 28 ns to about 34 ns in order to avoid the loss of charge collection due to inadequate integration time.

As the readout was data driven with no fixed length, the FIB used the last channel of the last chip in the chain to identify the end of a chip chain's data stream. Failure to detect this, which could be caused by the chip, DOIM, or FIB error, could potentially make the FIB wait for an indefinite amount of time. A timeout was added to the FIB to terminate readout and append an error code to the data stream.

Data were also initially lost to a race condition in the data concatenation algorithm at the VRB level. This condition shifted every other 4 bits in the data stream by 8 bits, leading to data corruption and the loss of events at the 1% level. Once the systematic shift was distinguished from random corruption, the VRB firmware was modified to eliminate this source of data loss.

### 3.6. Wirebond resonance: spontaneous loss of $r$ - $z$ sides in the double-sided ladders

Shortly after the beginning of data taking operations in 2002, 4% of the  $r$ - $z$  side of SVX-II ladders were spontaneously lost during operations. In the SVX-II, the  $r$ - $\phi$  and  $r$ - $z$  side hybrids of the ladders were connected with a set of wire bonds, known as the *jumper*. The jumper was perpendicular to the 1.4 T magnetic field produced by the CDF solenoid (Section 1). On every readout sequence of the chips, a varying current flowed through the jumpers, which resulted in a Lorentz force that induced a kick on the jumpers. This process usually did not lead to a resonant condition, as the readout commands were typically randomly spaced. However if the readout commands came at a fixed frequency, a resonant Lorentz force could cause the wire to break from mechanical fatigue. It had been shown that some resonant frequencies of the

jumpers were in the 10 kHz range (which exactly matched the CDF L1A trigger rate under certain conditions) and only a few kicks were necessary to excite the jumpers [13]. These resonant readout conditions would arise when there were synchronous L1As from calibration triggers, faults in the trigger hardware, and ladders with large and fixed length readout. The silicon detector was removed from all calibration triggers and faulty trigger hardware was replaced. L00 had large fixed readout, discussed in section 3.7, and its separation from the SVX-II readout (Section 3.7.1) was necessary to mitigate the resonances.

### 3.6.1. Operational mitigation

During the initial investigation, it was understood that the damage was correlated with the L1 trigger rate. The maximum L1 trigger rate was set to 20 kHz, where the typical peak rate was about 12 kHz. A limit was implemented in the DAQ software, called the *trigger handbrake*, that would halt data taking if the four-second-average of the L1 trigger rate exceeded the maximum rate. After the wirebond resonance was discovered and the Ghostbuster protection system was commissioned, the maximum rate was raised to 35 kHz. In addition, an administrative procedure required that every change to the trigger system was tested without the silicon detector and signed-off by the silicon operation group.

### 3.6.2. Ghostbuster protection system

Given that it only took a few kicks at a  $\sim 10$  kHz resonance frequency to excite a resonance, the *Ghostbuster* [33], already developed for SVT, was reprogrammed to detect the onset of a resonance condition within  $\sim 1$  ms. The Ghostbuster paused data taking as soon as a series of synchronous readout commands had been detected. The FFO was modified to send readout commands to the Ghostbuster. The addition of the Ghostbuster was essential to allow CDF and the silicon detector to acquire data at the highest L1 rates. Without the development of this board, the CDF physics program would have been severely limited. After the introduction of the hardware protection system, losses of the  $r$ - $z$  side in ladders due to resonant conditions were eliminated, except for two cases in 2005 and 2007 (Fig. 8). After the commissioning of the Ghostbuster, the trigger handbrake remained as a redundant limit on the L1A rate.

The Ghostbuster algorithm paused data taking when it appeared that the timing of readout commands was within a narrow frequency band. The Ghostbuster recorded the time interval between successive readout commands. A difference in successive intervals of less than  $1 \mu\text{s}$  was counted as a *tick*. If the difference in successive interval lengths was greater than  $1 \mu\text{s}$ , the tick counter was reset. A resonance error was declared when the tick counter reached a preset threshold, typically set to 11. The threshold value was initially determined from a Monte Carlo simulation of the DAQ, and tuned to running conditions when necessary. There was always a non-negligible chance that a set of consecutive random L1 triggers would look like a resonance, and the threshold set point was a compromise between detector safety and limiting false resonance alarms.

Fig. 7 shows the the number of resonances per week detected by the Ghostbuster during all of Tevatron Run II. The spikes in the number of resonances per week were mostly caused by faulty trigger hardware or long readout times for ladders. The typical rate, neglecting those originating from faulty trigger hardware, was about 10 resonance errors per week (1.4 per day) consistent with stochastic operation.

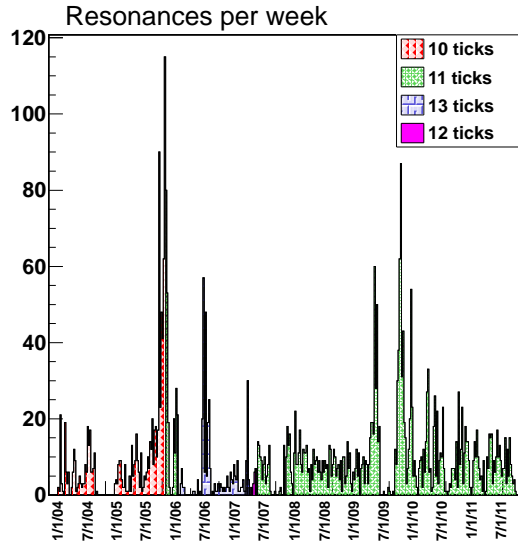


Figure 7: A historical account of the number of resonance per week detected by the Ghostbuster. The maximum number of ticks, which triggered the Ghostbuster resonance detection, varied from 10 to 13 ticks during Run II, and eventually settled at 11. The spikes in the resonance rate are mostly due to faulty trigger hardware. The typical resonance rate was 10 per week (1.4 per day).

As mentioned previously, any ladders with long fixed readout would exacerbate the likelihood of resonances at some L1 rates. The readout time could increase from corruption of the pedestal subtraction algorithm or if the noise level had grown. In both cases, the ladder readout time is no longer dictated by detector occupancy but rather ladder noise. This could lead to approximately fixed long readout times. Also some chips in a chip chain were switched to read-all mode to fix some errors, which also increased the readout time. During 2009-2010, the noise level in a handful of ladders had grown large enough, and consistent enough in length, that the number of resonances increased and gradually forced the peak L1 trigger rate to be limited to 25 kHz. The problematic noise growth was due to malfunctions in the chip or the sensor itself, and was several times larger than the noise growth due to radiation damage observed in most ladders. The noise was often isolated to a few chips of the chain, and by increasing the NN sparsification threshold of the affected chips, the noise was suppressed without compromising the data from other chips in the ladder. With

this noise suppressed, the peak L1A rate was increased to 32 kHz counts during normal data-taking, without creating resonances.

### 3.7. L00 noise

L00 was included to improve the precision of measuring displaced vertices that was essential for the discovery for  $B_s$  oscillations [34]. Unlike SVX-II and ISL, the L00 readout chips were not mounted directly on the L00 sensors to minimize the amount of material and so reduce the effects of multiple scattering. Instead, a fine-pitched cable connected the sensors to the readout chips.

After L00 installation, significant noise was observed on the L00 readout that manifested as large pedestals that varied across a chip and with each event, with the largest variation at the edges of the readout cables. These pedestals could not be removed by DPS. An investigation concluded the noise was picked up by the fine-pitched readout cables [11].

L00 was forced to operate in read-all mode and the pedestals were removed by an offline event-by-event correction. During the offline data processing, the recorded charge across a chip was fit to Chebyshev polynomials to extract the pedestal. Tests using simulation were performed to check for biases from fitting and none were found [11].

#### 3.7.1. Two-SRC mode

The original silicon DAQ read out SVX-II, ISL and L00 together. A consequence of operating L00 in read-all mode was that it had the largest data volume and was fixed length, which exacerbated the wirebond resonances (Section 3.6). As L00 and ISL were not used by SVT, they were separated from SVX-II DAQ and read out by a separate SRC after a L2 accept. This improved the readout time and also mitigated the wirebond resonances.

#### 3.7.2. Load balancing

During Tevatron Run II, the peak instantaneous luminosity increased from  $50 \times 10^{30} \text{ cm}^{-2}\text{s}^{-1}$  to  $400 \times 10^{30} \text{ cm}^{-2}\text{s}^{-1}$  and this had two consequences: higher detector occupancy and an increased trigger rate. Without improvements to CDF's trigger and DAQ, CDF would not have been able to operate at this high instantaneous luminosity. In particular, some data segments arriving at the event builder were significantly larger than others, and the event builder performance was limited by the largest of these data segments. To mitigate this effect, the number of VRB crates was expanded for both silicon and non-silicon systems, and data rates were equalized across the crates.

As described in Section 3.4, data from the CDF silicon detector was buffered on VRBs until a L2 decision arrived. Each VRB crate was read out in parallel and the total readout time was dictated by the L00 VRB crate as it had the largest data volume. The L00 VRB crate had a fixed event size of 28kB per event as a consequence of its read all mode (Section 3.7).

The readout time was reduced by mixing ISL and L00 VRBs to balance the data volume across VRB crates, thus reducing the peak data volume per VRB

crate. A configuration was found and implemented during the 2006 Tevatron shutdown. The maximum event size of a single crate reduced from 28 kB to 20 kB.

Despite the success of the load balancing, the increased instantaneous luminosity of the Tevatron forced another re-optimization of the CDF DAQ. For the silicon DAQ, balancing the load across VRB crates was no longer sufficient. An additional VRB crate was added to the L00/ISL readout and remained in operation until the end of Run II.

### *3.8. Operational experiences and improvements*

The commissioning of the CDF silicon detector was completed at the start of 2003 and the detector was included safely in normal data taking. This section describes the routine day-to-day problems that persisted to the end of Run II. The issues that affected the silicon DAQ on a daily basis were broadly categorized as effects from single-event-upset and bit errors. Procedures were developed to resolve common problems but required constant vigilance by the detector operations shift crew. Another issue, which persisted, was the full-detector trips, where either subdetectors, or the complete silicon detector would switch off. Although far rarer, typically four times per year, it took 45-60 min to recover and resume data taking. Another large component of detector operation was the daily maintenance of the 580 ladders and 5644 readout chips. With such a large number of components, at least one readout chip and/or ladder required some daily adjustment.

#### *3.8.1. Impact of ionizing radiation*

A sizable fraction of the DAQ system was installed in the CDF collision hall, which was subjected to radiation from the Tevatron's colliding beams. As a result, the majority of electronics failures were due to radiation induced single event upsets (SEU). A SEU is a change of state caused by radiation striking a sensitive component in an electronic device. The change of state is a result of the free charge created by ionization in or close to an important logic element or memory bit.

During Run II, the Tevatron substantially reduced radiation rates, thereby reducing the radiation induced failures. At the end of Run II, the rates were so low that they fell below the detectable threshold of the radiation monitoring counters during the course of a Tevatron store. Also, the introduction of the Silicon-Autorecovery (SAR) in 2008 automated the detection and recovery of these SEU failures of the DAQ and the power supplies. It reduced interruptions to data taking from 10-20 min to less than 5 min.

*Reinitialization of chip chains.* During data taking, the current consumed by the analog FE of a SVX3D chip chain (Section 3.3.1) could spontaneously drop by 80-100 mA, implying one chip in the chain was not recording any data. This typically occurred at rate of once or twice a day. A program dedicated to monitoring the power supplies sent an alarm to the DAQ if such a drop in chip current was detected, and the data taking was paused for less than a minute

to reinitialize the chip chain. Overall, this only had a minor impact on data taking.

*FIB bit errors and FIB FPGA burnout.* Each FIB had 16 FPGAs, and thus a higher rate per board of SEU damage than the other VME modules. Data corruption errors were resolved by reloading the FPGA programs of the affected FIB, which typically occurred 1-2 times a day. On rare occasions (3-4 per year), one of the FPGAs would enter a high current state and blow a fuse on the board. In a majority of cases the affected FPGA had to be replaced, and in the remaining cases, a reprogramming of its firmware was needed.

### 3.8.2. Bit errors in the data stream

As the silicon DAQ is data driven, the data format had to be self-describing to identify not only the amount of charge but also the location where it was recorded. Therefore any corruption of the data implied more than just errors in digitization. During operations, several sources of bit errors in the data stream were detected and immediately addressed. While some errors, especially those from on-detector components, could not be repaired, many could be corrected in the offline reconstruction. Operating the SVX3D readout in nearest-neighbor mode guaranteed at least three consecutive strips would be read, and the error-correction algorithm could exploit this feature to identify and correct single-bit errors.

*Bit errors in the optical links.* One common instance of bit errors in the data stream was in the DOIM system. At the start of Tevatron Run II, most DOIM bit errors were traced to bad electrical contacts in the sockets that held the RX in the FTM. Gold plating the pins of those devices to establish a better connection with the sockets eliminated this source of bit errors.

During Tevatron Run II, the typical DOIM bit errors manifested as bits that were stuck low or high in the data stream, which corresponded to either a malfunctioning RX unit or TX unit. Faulty RX units were accessible and replaced from a pool of spares when necessary. Faulty TX units were inaccessible and thus irreplaceable. Some TX failures could be recovered by adjusting power supply settings to tune the TX unit light output. Another class of TX-related errors were linked to bad connections in a circuit board which served as the interface between the sensors and the power supplies. These boards were located just outside the tracking volume and were accessible only when the Tevatron was shut down for at least a week. In these instances a borescope and a custom tool were used to push the circuit board back into place to re-establish the electrical connection.

*Bit errors in the readout boards.* The FIB occasionally caused bit errors in the data stream, most commonly due to SEUs and component failures. SEU related bit errors were resolved by reloading the programs to the FPGAs on the boards. FIBs boards with failed components were replaced. On rare occasions (less than once per year), VRB boards gave bit errors that were traced to component or printed circuit boards failures and were replaced.

### *3.8.3. Full detector trips*

There were several incidents in which most or all SVX3D chips in the silicon detector would go into a high current state leading to power supply trips. These trips occurred in some or all of the SVX-II, ISL, and L00 sub-detectors and occurred more frequently in the winter season. On average, it took about 45-60 min to recover from these incidents.

Only some of the sources of these trips were reproducible and the remainder were hard to diagnose and resolve due to their rarity. While the origin of all these trips was unknown, many potential causes were identified and eliminated as sources of the problem. It was observed several times that personnel working near the electronics area could induce this problem, suggesting that loose or corroded contacts may have been a source; the re-seating and replacing of many key components proved inconclusive. It was also suspected that differences in grounding levels between the racks could generate this problem, but no evidence of a bad ground was found. Another of these sources was the corruption of the clock signal and consequent lack of keep-alive commands sent to the chip, as detailed in Section 3.5.1. The underlying reasons for corrupted clock inputs were not clear, and many full detector trips did not show any indication of clock corruption.

It was found that some of these trips did occur in coincidence with a high-voltage power supply trip of one particular muon detector chamber. The muon detector chamber was powered with 3500 V and had a current draw of about 1 mA. The trip of its power supply during these incidents was attributed to arcing between the high-voltage lead and the chamber ground. The hypothesis that an arc in a completely unrelated subsystem would give rise to a massive power trip in the silicon detector was tested by inducing an arc in the muon detector chamber and observing the behavior of the silicon detector. The arc was forced by closing in the high-voltage lead to the ground until a spark was generated, and full subdetector trips in the silicon detector were reliably reproduced each time the spark was induced. The mechanism was believed to be electromagnetic pickup between the muon chamber high voltage distribution cables and the clock crate during the occurrence of the spark. The electromagnetic field bursts were observed by carefully-placed coils in the surroundings of the clock crate. The pickup induced a change in the ground level of the clock signal, which exceeded the specification for the silicon electronics, resulting in an effective lack of clock signal during a period of time of about a few microseconds; thus no keep-alives were sent during this clock interruption. This problem was solved by reducing the voltage applied to the defective muon detector chamber to 3200 V.

### *3.9. Summary of DAQ performance*

The CDF silicon DAQ was very complex in order to meet the challenges of providing data to SVT. Its performance during Tevatron Run II was defined by three major phases: commissioning (2001-2003), steady operations (2004-2008), end of Run II (2009-2011). The long commissioning period was directly due to the large number of unexpected problems that were apparent only after

installation of the silicon detector. The challenge of tackling these problems simultaneously (in addition to a number of non-DAQ issues), while attempting to take data simultaneously was considerable. However after this commissioning period, the silicon DAQ entered a stable period and efforts to optimize the performance and operations were carried out, in addition to daily maintenance of the DAQ components. From 2009, the dwindling pool of working spare components and the effects of radiation were taking their toll.

Figs. 8 and 9 are historical records of the different types of errors accrued by the DAQ electronics during Tevatron Run II, expressed as the fraction of bad readout chips. Fig. 8 shows the SVX-II  $r$ - $\phi$  and  $r$ - $z$  sides separately. The definition of the different errors are:

- *AVDD2*: SVX3D errors diagnosed as AVDD2 type errors (Section 3.5.1)
- *SVX3D*: SVX3D errors that are not AVDD2 type error (Section 3.5.1)
- *Detector*: Faults which originate in the silicon sensor
- *Optical*: Errors which are from DOIM TX or RX
- *Jumper*: Ladders whose  $r$ - $z$  side was lost from wirebond resonances (Section 3.6)
- *Cooling*: Ladders turned off due to lack of ISL cooling (Section 5.2.1)
- *Hardware*: Error and faults which do not match any of the categories defined above

During the commissioning phase, the number of bad chips (ladder) grew as the different problem manifested, then stabilized in 2003 (steady state running). The  $r$ - $z$  plots in Fig. 8 shows that there were only 4 additional jumper failures after the inclusion of the Ghostbuster and none of these was an immediate consequence of beam incidents or resonant conditions. After the inclusion of the Ghostbuster, data were taken safely and reliably with peak L1 trigger rates in excess of 25 kHz - essential for CDF physics. The failure rate of chips after 2003 is far lower compared to the commissioning period. Most of the different failure categories stabilized. From 2009, the chronic effects of radiation damage and aging were starting to take their toll on the silicon detector. The failures from SVX3D and optical were steadily increasing and half the total radiation dose was delivered between 2009 and 2011. With the increased radiation, components started failing more often, shrinking the pool of spare components. These plots also highlight other problems of the silicon detector that affected the DAQ. Fig. 9 shows a large rise and fall in the fraction of bad ISL chips during 2003 due to blocked cooling line and its eventual clearance; this is discussed in further detail in Section 5.

At the end of Run II, 84% (73%) of all SVX-II  $r$ - $\phi$  ( $r$ - $z$ ) and 89% of all ISL SVX3D chips continued to function without error and did not compromise the silicon detector tracking performance. This is an impressive feat as the CDF silicon was designed to be replaced after the first  $2\text{-}3 \text{ fb}^{-1}$ , about three years.



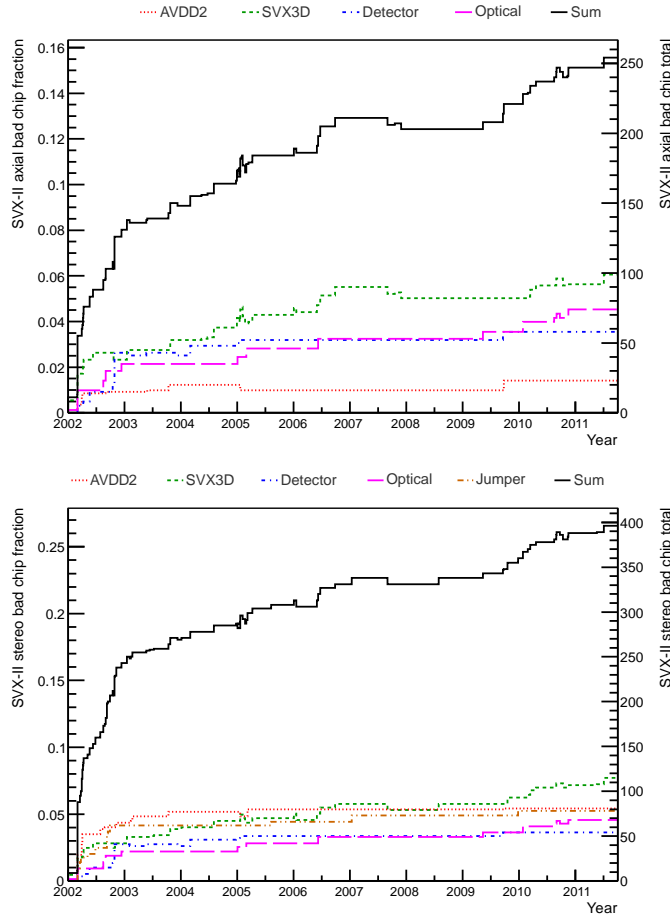


Figure 8: A historical account of the different errors and faults accrued by the SVX-II  $r$ - $\phi$  (top) and  $r$ - $z$  (bottom) SVX3D chips during Tevatron Run II. Each error category is defined in Section 3.9. At the end of Tevatron Run II, 84%  $r$ - $\phi$  and 73%  $r$ - $z$  SVX chips were still operating without error.

It survived four times the radiation dose and lasted three times longer than the original design.

#### 4. Power supplies

The CDF silicon detector used power supply modules manufactured by CAEN. A total of 114 custom modules were housed in 16 SY527 mainframe crates located in the corners of the CDF collision hall. The crates were elevated 2-7 m off the floor due to space constraints in the collision hall. This location had a distinct disadvantage; the supplies and crates were continuously exposed

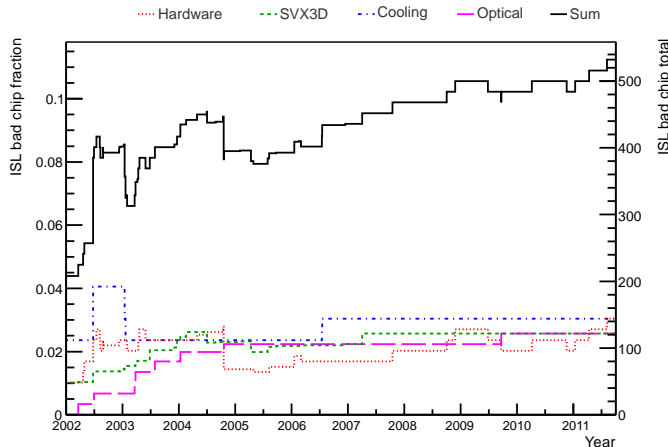


Figure 9: A historical account of the different errors and faults accrued by the ISL SVX3D chips during Tevatron Run II. Each error category is defined in Section 3.9. At the end of Tevatron Run II, 89% of ISL SVX3D chips were still operating without error.

to radiation, which not only shortened the life of many internal electronic components, but also resulted in single event upsets that required a crate reset and in single event burnouts that necessitated additional hardware protection for the detector. Investigation or replacement of a problematic power supply required access to a radiation controlled area for 1-2 h.

#### 4.1. System overview

One power supply module provided low voltages (2 V and 5 V) to the port-card, low voltages (5–8 V) to the SVX3D chip chains, and high voltage (up to 500 V) to bias the sensors of one wedge of the silicon detector. The low voltages were set via potentiometers on the side of the supply, while the high voltage was set via software on the SY527 crate. All channels had a maximum voltage setting. If the channel voltage exceeded its maximum, an “overvoltage” error was met and the power supply cut power to the affected channel. These limits were also set via potentiometers on the modules. Any adjustments to the low voltage or the maximum voltage settings had to be done with the supply inserted into the crate and the crate powered. Because of this need and the location of the potentiometers, changing these settings were not possible in the collision hall, rather it had to be done on a test stand, using a specially modified crate.

The SY527 crate had an RS-232 interface for connection to a computer, as well as a Lemo input to reset the crate remotely. In addition, the crate had a proprietary serial communications port, which connected to a V288 high speed CAENet VME Controller. The V288 connected to another controller card in the same crate which had an ethernet port for external communications. A VME crate was used to communicate with all the crates in the collision hall this way, and a Java program provided a graphical interface of the power supply controls.

A PC monitored and logged parameters, including power supply voltages, currents, and the time of last communication for each power supply crate. This PC logged parameters for the cooling system as well (see Section 5).

#### 4.2. Decreasing low voltages

In 2005, after over 4 years of data taking, low voltage channels of several power supplies were found to drift erratically from their nominal values. Specifically, filter capacitors in a particular regulator circuit of each low voltage channel gradually lost their capacitance, causing the low voltage supplied by the circuit to drop over time, typically a tenth of a volt over the course of three months. Left unchecked, this could cause the readout electronics to stop working.

The solution was to replace all of the filter capacitors (32 in total) on the supply. This repair was done on-site at FNAL, and typically only took a few hours. The swaps were usually not urgent (the readout electronics would still work at 0.5 V below nominal), and were done when another problem in the detector required an access to the collision hall. Fig. 10 shows the analog low

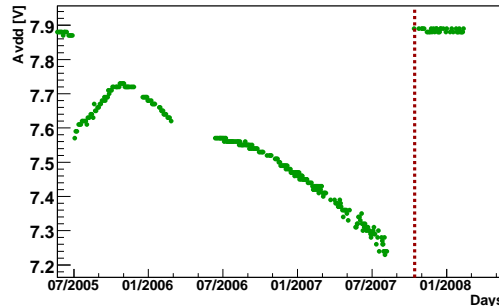


Figure 10: An analog low voltage line powering a series of SVX3D chips of an SVX-II ladder is seen dropping gradually over time. The vertical dashed line marks the replacement of the faulty power supply.

voltage channel of an SVX-II ladder drifting over a period of two years. The vertical dashed line marks the time when the faulty power supply was replaced, restoring the low voltage to its nominal value. The gaps in the plot correspond to Tevatron maintenance shutdowns. During the 2007 (2009) shutdown 47 (21) supplies out of a total of 112 were repaired and replaced. Most of the remainder were replaced gradually a few at a time utilizing the spare pool in hand.

#### 4.3. Single event upsets

A consequence of the power supplies being located in the radiation environment of the collision hall was that both the crates and supply boards were subject to single event upsets. This typically only required the crate to be reset. Even so, every reset cost a few minutes of data acquisition time.

The SY527 crates had a Lemo input for remotely resetting the crate; the reset cable ran from the crate to the counting room outside the collision hall. Thus, the shift crew could reset the crate when necessary, although the procedure, from identification of a problem to manually turning the supply on again, took about 10 min. In order to eliminate any delay due to human intervention, an automatic system was developed to detect when a particular crate has stopped communicating its voltage and current readings. Once this state was detected, the automatic reset system sent the reset signal to the crate. The supplies had to be turned on again once the crate had rebooted. Recovery from an automatic crate reset was automated with the development of Silicon Auto-Recovery, described in Section 8.1, which reduced the downtime from such incidents from 10 min to less than 5 min.

The supplies themselves were also subject to radiation induced effects. Specifically, certain power metal oxide semiconductor field effect transistor (MOSFET) components of the L00 supplies underwent single event burnouts (SEBs) [35], causing the supply to output its maximum bias voltage. If this were to happen with the detector connected, it could result in permanent damage to the silicon sensors. Fortunately these SEBs were first observed during commissioning, before the detector was connected.

In order to prevent potential damage, compact voltage fuses, called *crowbars*, were developed and installed. The crowbars interrupted the current if the bias voltage exceeded a specified voltage. They were placed between the high voltage detector cable and the supply itself. The initial crowbars protected the sensors from bias voltages above 150 V. In 2008, when radiation damage necessitated operating at larger bias voltages, new crowbars with a voltage limit of 450 V were installed.

#### *4.4. Operational experience*

Ten years of experience in operating the power supplies helped the detector operation crew identify potential problems and react to them before they caused significant downtime. Many improvements were made, mostly to the procedures used to test supplies after repair or work in the collision hall.

##### *4.4.1. Testing procedures*

All the repaired supplies were run through a series of tests, designed to mimic the operating conditions in the collision hall, before their installation in the detector. These included long periods of being powered on (burn-in), as well as rapid power cycling. The former were crucial to detecting intermittent problems.

The testing procedure consisted of connecting the supply to a set of static impedance loads (a loadbox), and turning the supply on for approximately 24 h. It was followed by a test that turned the module on and off every 2 min for approximately 24 h. The currents and voltages read out in each cycle were analyzed to ensure stability.

If a module was forcibly switched off for its protection (“tripped”) during the first 24 h or any currents or voltages were unstable during the second, the

module was sent for additional inspection or repair. The safety features of the module were also tested to verify it tripped properly under limiting conditions of voltage and current and when the supply enable signal was absent.

In addition, the power supplies were tested in the collision hall just before their deployment in the detector. The procedure to check out a supply in the collision hall consisted of connecting it to a loadbox and turning it on. Currents and voltages as read back from the module were recorded, and voltages were measured and compared at the loadbox. The safety features were tested again to make sure that the supply tripped off at intended voltage and current conditions. Then, the supply was connected to the sensors, and turned on. Given the location of the crates, the RS-232 interface provided the optimal method of testing, as it allowed easy control of the module using a laptop on the collision hall floor.

The loadbox was made by the Computing Division ESE at FNAL and incorporated different load resistances for L00 and SVX-II/ISL supplies with capability to switch between them. It utilized an ADC to automatically measure the voltages on each channel. With the loadbox, the collision hall check-out procedure was quick, reliable and reproducible.

#### *4.4.2. Damage to power supplies during transportation*

When power supply modules could not be repaired on site, they were sent back to the manufacturer in Italy. Shipping the modules back to Fermilab damaged more than half of the shipped power supplies. In 2008, a short study was done to examine the shipping method adopted by the manufacturer and implement improvements to prevent future breakage.

In order to streamline the transit and prevent breakage, a set of procedures was devised for the manufacturer to follow when shipping supplies back. First, instead of routing via CAEN's business office in New York, the modules were required to be shipped on a direct flight from Italy to Chicago. Second, the supplies were to be shipped on a standard shipping pallet, requiring the use of a forklift to prevent the box from being mishandled. Finally, an accelerometer inside the box and shock/tilt sensors affixed to the outside of the box were used to monitor the detailed motion the supplies were subjected to while in transit. Using these procedures, every supply that was shipped back to Fermilab arrived in working order.

## **5. Cooling system**

### *5.1. System overview*

The sensors had to be kept chilled at all times in order to prevent migration of radiation-induced defects, which shorten the working lifetime of the detector, and to reduce the sensor leakage current, which increases with radiation damage.

The SVX-II, ISL, and L00 detectors were cooled by two closed-circuit liquid cooling systems. One system, shown in Fig. 11, was used to cool SVX-II and

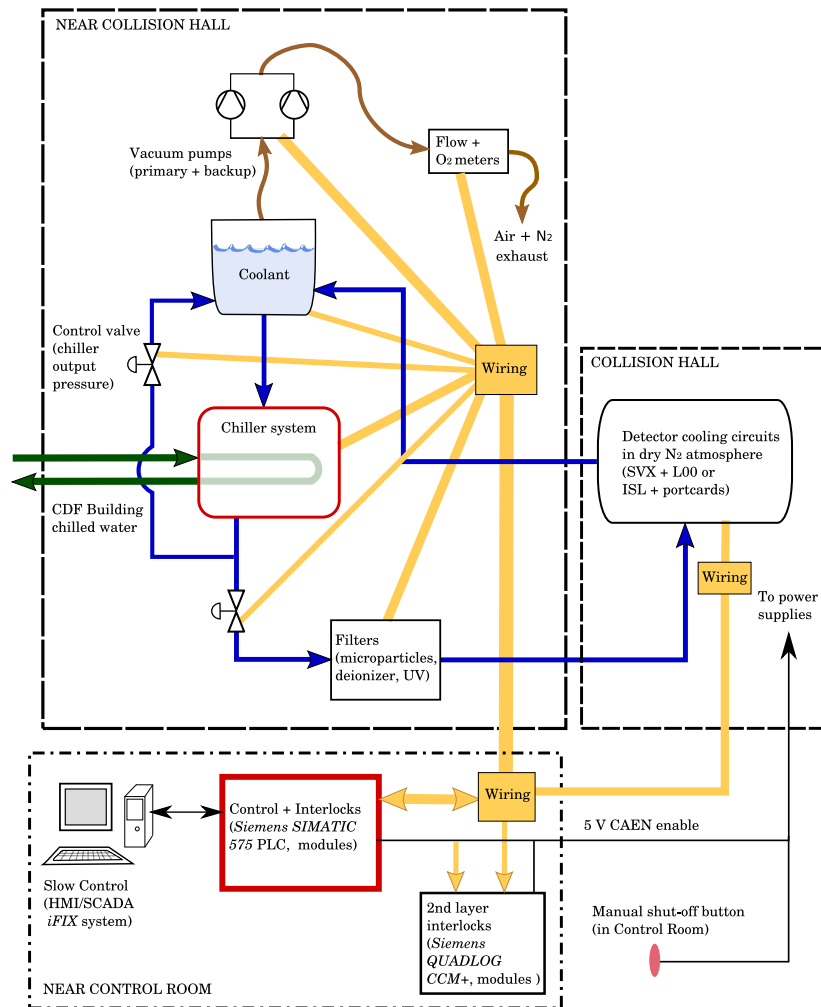


Figure 11: Schematic of the SVX-II/L00 cooling subsystem. The subsystem for ISL can be described in the same manner, though both subsystems share the same PC and control/interlocks crates.

L00. A second separate system was used for ISL, although some of the cooling control electronics and interlocks were shared.

Due to the higher radiation levels close to the beam line, the operating temperature of L00 and SVX-II was chosen to be lower than ISL. The temperature of the coolant out of the chiller was  $-10^{\circ}\text{C}$  for SVX-II/L00 and  $+6^{\circ}\text{C}$  for ISL. The coolant for SVX-II/L00 was a mixture of 30% ethylene glycol and 70% water by weight, and the coolant for ISL was distilled water. Both coolants warmed up by a degree or two in the piping between the chillers and the detector. The total cooling load for SVX-II/L00 during operation was approximately 5 kW, and that of ISL is approximately 4 kW. About half of this heat load was produced by the silicon detector and the remainder was heat transferred from the warmer surroundings. Most of the heat generated by the silicon detector was produced by the SVX3D readout chips. All of the portcards were cooled by the ISL system because the temperature of the ISL system was within the range of the optimal performance of the light transmitters. In order to prevent water from condensing on the sensors and electronics, dry nitrogen flowed through the silicon detector volume.

In the SVX-II ladders, the electrical hybrids were cooled through thermal contact to beryllium support bulkheads, with integrated cooling channels. For L00 and ISL ladders, and for the portcards, cooling was achieved through thermal contact to aluminum tubes glued to the mechanical supports. The SVX-II and ISL sensors were not in close thermal contact with the coolant, however, nor were their temperatures directly monitored. Based on the measurements of the ambient temperatures and the bulkhead temperatures and on thermal models, we estimated the temperatures of the sensors while the detector was powered to be between 0 and  $10^{\circ}\text{C}$  for SVX-II, and between 15 and  $25^{\circ}\text{C}$  for ISL. The L00 sensors, however, were in close thermal contact with the coolant tubes, and their temperature was about  $-5^{\circ}\text{C}$  when powered.

In order to prevent damage to the electronics if a coolant pipe leaked, all cooling pipes were operated below atmospheric pressure so that a leak in a pipe or a fitting would draw nitrogen into the cooling system rather than leak coolant into the detector volume. The cooling system had vacuum pumps and air separators in order to maintain the sub-atmospheric pressure in the system at all times. Two vacuum pumps were available per system, with one running and one piped in as an immediately available spare, switchable with electronically controlled valves.

The coolant was circulated by pumps on the two chillers: one for SVX-II/L00, and one for ISL. A third chiller was available to be used as a spare in case of failure of either chiller. This system was used successfully in November 2004, when the spare chiller was used for two days while a leak in the ISL chiller was identified and fixed.

Each of the SVX-II/L00 and ISL chiller circuits had a set of filters — a microparticle filter, a UV sterilizer to limit biological activity in the coolant, and a resin-cartridge de-ionizer. The conductivity of the coolant was regulated to be approximately  $0.6\ \mu\text{S}/\text{cm}$ . The pH of each of the two coolants was monitored via weekly samples drawn from the air separators and both stayed near a pH of

6.

To ensure the safety of the silicon detector, a series of interlocks prevented the power supplies from being turned on when insufficient cooling was available, and coolant flows were switched off if an unsafe situation existed. If the pressure in any of the cooling lines rose to within 1 psi of atmospheric pressure, electrically controlled solenoid valves on the coolant supply lines to the affected detector subsystem were shut automatically. If dewpoint sensors detected that the dewpoint was within 3°C of the minimum temperature in the detector volume, then flows were shut off.

The interlock system had the ability to disable power to the detector. The CAEN power supply modules required a voltage of +5 V in a Lemo connector in order to enable detector power. Dropping of this +5 V had the effect of switching the power off. If there was insufficient flow of coolant to the detector or if temperature sensors indicated that a coolant temperature was too high then the detector power supplies are turned off via the +5 V control lines. The electronics crates that housed the CAEN modules monitored the temperature of the electronics and the status of the crate fan pack, and would shut off if a failure was detected.

These interlocks were controlled by a Siemens SIMATIC 575 Programmable Logic Controller (PLC) [36], attached to two crates containing modules that read out temperature, pressure, and flow transducers. A third crate provided control for the solenoid valves, the vacuum pumps, the chillers, and the 5 V power supply enable lines.

A second layer of interlocks was provided by a Siemens QUADLOG CCM+ PLC [37]. This controller had an independent readout of the coolant flows and pressures and also monitored the state of the power supply interlocks. If power supplies were permitted to be turned on but coolant flows were too low (< 1 LPM) — which could only happen if the first PLC's interlocks had failed — this interlock system would turn off the power to the silicon power supply and FIB racks (section 3). The QUADLOG system also protected against over-pressure conditions — again in the event of a failure of the first PLC system — by shutting down coolant flows.

During a power outage, backup systems kept the cooling system functioning at a reduced level. Power was supplied to the PLCs and control electronics from an uninterruptible power supply (UPS), which was backed up with a diesel generator. The vacuum pumps were powered by the diesel generator but not the UPS, and therefore they did not pump during the time required for the diesel generator to start up at the beginning of a power outage, but resumed pumping shortly into the outage. CDF's building water chillers did not operate during a power outage, and so a dedicated air-cooled backup chiller, which was powered by the diesel generator, was able to supply chilled water to the SVX-II/L00 chillers. The ISL chiller's compressor did not operate during a power outage, but a backup coolant pump maintained coolant circulation.



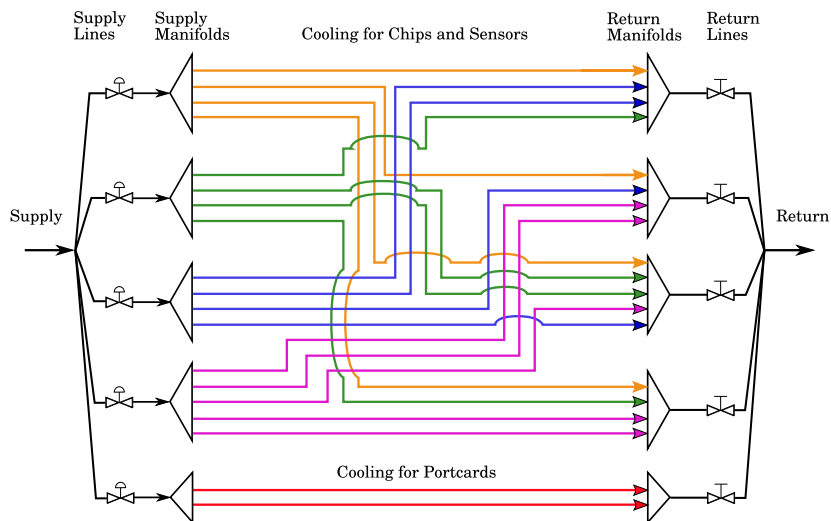


Figure 12: Diagram of the connections of the cooling lines of the east half of ISL showing the supply and return manifolds located in the detector frame. Flow which enters the detector via one of the four supply lines was shared among several return lines. Electronic supply valves and manual return valves are shown.

## 5.2. Operational experience

The cooling and interlock system for the CDF silicon detector had a high reliability and failed infrequently. The main goals of protecting the silicon detector and preventing any damage to other detectors were well fulfilled. However, a few major incidents affecting the ISL cooling structure inside the detector revealed the inadequacy of the interconnected branching scheme of the cooling piping (see Fig. 12). Isolation of leaky segments (Section 5.2.3) was very difficult and required a multi-week shutdown of the detector. During these down times a great deal of work was invested to investigate and repair leaks. In contrast, the SVX-II/L00 cooling system, which had a simpler geometry, was more stable and performed better.

### 5.2.1. Blockage of cooling flows in ISL

When the ISL detector was commissioned, it was discovered that 35% of the lines in ISL were not cooling. Further investigation using long borescopes showed that the coolant flow was blocked by epoxy found at aluminum right-angle elbows in these cooling tubes. In 2002 and 2003, these blockages were opened by shining Nd:YAG laser light to vaporize the epoxy. A pulsed laser operated at an average power of 10–40 W was used, guided by an optical fiber with a 400  $\mu\text{m}$  core and a 20  $\mu\text{m}$  Al jacket. The fiber was attached at the end to a device holding a prism at a right angle so that the laser light could be aimed at the epoxy plugs just beyond the bends of the elbows.

This operation was delicate and difficult, as the coolant piping had an inside diameter of 4 mm and the elbows were approximately two meters away from

the accessible end of the tubing. One cooling line was found to be extremely difficult to open and during the attempts the prism holder became detached from the fiber and remained lodged inside the pipe. The flow in the line was not restored, and a concern of leaks developing due to stagnant coolant with corrosive ions building up made it prudent to plug the narrow tube. Aluminum plugs were inserted at the manifolds where the cooling supply and return lines divide into four or five narrower tubes. A second prism holder was stuck in another narrow tube and repeated attempts to remove it failed. This reduced the flow, but did not block it.

The successful opening of the blocked ISL flows raised the fraction of working ISL cooling lines from 65% to 96%.

### *5.2.2. Degradation of coolant and corrosion*

In 2005, the SVX-II chiller setpoint was lowered from  $-6^{\circ}\text{C}$  to  $-10^{\circ}\text{C}$  in order to extend the longevity of the silicon detector. After this change to the operating temperatures, there was an incident during routine maintenance work on the ISL vacuum pump that accidentally fired the safety interlocks of the cooling system. This stopped the flow of ISL coolant for at least 30 minutes. The ISL cooling system also serves as the cooling for the portcards for the entire silicon detector and during this period, the coolant in the SVX-II portcard cooling lines began to freeze due to their proximity to the SVX-II cooling system which was at  $-10^{\circ}\text{C}$ . This constricted the flow of coolant in the SVX-II portcard lines to less than the accepted minimum rate for the safety interlocks which in turn did not permit the SVX-II detector to be powered. The frozen coolant in the SVX-II portcard line was melted by raising the SVX-II coolant temperature from  $-10^{\circ}\text{C}$  to  $+6^{\circ}\text{C}$  and turning the ISL on to raise the ambient temperature. After two hours, flow was reestablished to the SVX-II portcard lines which allowed the SVX-II detector to be powered. In order to prevent freezing incidents, which risk portcard line ruptures, 10% of ethylene glycol by weight was added to the ISL coolant.

In 2007 the pressure in an ISL portcard supply line rose beyond the operational tolerance due to leaks in the aluminum manifold which distributes the coolant to the portcards. Sufficient flow could not be maintained to cool the silicon sensor readout electronics and the east half of the detector had to be switched off. The investigation found that the pH of the ISL coolant had dropped to approximately 2.0. The conductivity had risen from  $2\ \mu\text{S}/\text{cm}$  to around  $3000\ \mu\text{S}/\text{cm}$ . Unfortunately, the conductivity meters at that time saturated at values far below  $3000\ \mu\text{S}/\text{cm}$ . An analysis based on ion chromatography revealed that the ethylene glycol had degraded into light organic acids, mainly formic acid at a concentration of  $12.5\ \text{g}/\text{l}$  ( $0.265\ \text{moles}/\text{l}$ ). Another analysis ruled out the possibility of microbial-induced degradation. There was evidence that warming up the ISL detector to  $13^{\circ}\text{C}$  during a two month shutdown in the summer of 2006 accelerated the acidification in correlation with the rise in conductivity. Several system components corroded faster than others with this degraded coolant. Outside the detector, the brass valve stems of the solenoid flow control valves had corroded, causing failures in the valves weeks before the

operational collapse. The portcard manifolds were made with aluminum 5052 piping welded using aluminum 5356 filler [38]. The filler material had corroded more quickly than the piping material.

The system was successfully repaired during a shutdown in the summer of 2007. The repair work involved inspection of the system with a borescope. The affected manifolds were located at a distance of 1 m inside the cooling tubes. With the use of a custom-made tool, Scotch DP190 epoxy [39] was laid down on the welded area of the leaking manifolds. In order to prevent corrosion the coolant was replaced by deionized water, and the pH and conductivity were monitored frequently in order to identify and mitigate hazards quickly. Through the remainder of Run II, the pH and conductivity were stable, and the affected portions of ISL were cooled.

The +6 °C cooling water supplied to the portcards and the heat generated by the portcards when powered were sufficient to keep the water from freezing during normal detector operation. When the portcards were not powered, however, a freezing hazard existed. Protection against freezing (the original impetus for adding glycol to the ISL coolant) was implemented via an interlock that inhibited flow to the SVX-II when the temperature measured in any portcard coolant circuit fell below 1 °C.

### 5.2.3. Leaks in ISL

The overall leak-rate of the ISL coolant system increased steadily after installation. The leak rate, as determined by the amount of time it took to leak up to atmospheric pressure when the vacuum pumps were valved off, increased by a factor of five between 2007 and 2009, prompting a third intervention to extend the longevity of the ISL cooling system. The aluminum ladder-cooling tubing was found to be leak-tight, except for a few smaller leaks in two tubes. The epoxied joints between polyethylene tubing and the aluminum manifolds where the small aluminum cooling pipes join were found to be the leakiest in the system. Additional epoxy was applied to three of these joints, and the flow performance improved, but the overall nitrogen leak rate remained at comparable levels as measured by the exhaust flow rate out of the vacuum pump. The flow rates and cooling performance were monitored closely for the remainder of CDF's data-taking run, and did not degrade to the point of requiring a change in the operation of ISL.

## 6. Particle beam incidents and monitoring

The particles from standard Tevatron running conditions (physics runs with proton-antiproton collisions) were responsible for the vast majority of the radiation dose to the CDF silicon detector sensors and components. However, beam instabilities and sudden beam losses were an unavoidable part of running a large accelerator, and posed a threat to particle detectors. As described in Section 2, the silicon detector was the closest to the beam and suffered larger consequences than the other CDF sub-detectors. Beam incidents early in Run

II resulted in large and acute radiation fields that permanently damaged about 4% of the readout chips in the detector. A two-pronged approach was taken to reduce the possibility of additional damage from beam incidents: a thorough review of past incidents and a strict beam monitoring system.

### 6.1. Particle beam incidents

When a beam incident occurred, a thorough review of the problem, in collaboration with the Fermilab Accelerator Division, often resulted in stricter testing of any hardware involved in the incident, as well as procedural changes in accelerator operation. The following list briefly describes the main types of beam incidents and the measures taken to lessen their impact.

#### 6.1.1. High beam losses

Particles leaving the outer halo of the beams at CDF (beam losses) were measured by counting hits in scintillation counters located on both sides of the detector. The counters were gated to exclude hits coincident with proton-antiproton collisions at the center of the detector. High losses at any time were indicative of higher radiation fields in the detector volume. More importantly, sudden changes in the losses indicated potential instabilities in the Tevatron beam. Monitoring software, described in Section 6.2, would automatically ramp down the silicon sensor bias voltage after dangerous beam conditions were detected. Under exceptional circumstances when the radiation increased dramatically, fast hardware protection systems would issue an abort which immediately removed beam from the Tevatron (Section 6.2).

#### 6.1.2. Kicker magnet pre-fires

A set of 10 *abort kicker magnets* were used to remove the circulating proton and antiproton beams from the Tevatron by steering them into a beam dump. The abort kickers have a finite rise time, so any beam which passed through those magnets as their field ramped up were not cleanly extracted into the beam dump. The beam train structure contained an unpopulated  $1.4\ \mu\text{s}$  gap, known as the *abort gap*, to allow the abort kickers to ramp up without affecting circulating beam.

Normally, beam aborts were synchronized with the abort gap so that the kickers would reach nominal field before the first bunches arrived to be sent to the dump. Occasionally, one of the 10 thyatrons that powered the individual abort kickers would trigger spontaneously. When such a *pre-fire* was detected, the other abort kickers were fired intentionally, without synchronizing to the abort gap, in order to abort the beam as quickly as possible. Any beam that passed through the pre-fired and other kicker magnets before they had reached nominal field could continue traveling with a distorted orbit, possibly hitting accelerator components and creating secondary and tertiary showers of particles at the experiments. The location of the abort kickers relative to the detector made CDF susceptible to large, acute doses from proton initiated showers. One such incident in 2003 resulted in the loss of about 4% of the silicon readout

chips. After a thorough review of the incident, a new collimator was installed to intercept protons that would strike the CDF detector due to an abort kicker pre-fire. Although pre-fires continued to occur several times per year, after the installation of the new collimator, the silicon detector did not sustain significant damage from such incidents.

### 6.1.3. Quenches

A quench is the sudden transition of a superconductor from a state with zero electrical resistance to a normal state with small, but finite, electrical resistance. For superconducting magnets like those in the Tevatron, a quench could be caused by a temperature rise of the current-carrying superconducting cable above its critical temperature. This could be caused by localized beam losses in the magnet or a loss of cryogenic cooling. An automated quench protection system protected the magnets from potential damage caused by the sudden ohmic heating, generated by the large current powering the magnets when resistance became normal. The quench protection monitors (QPMs) monitored the resistive voltage across a string of several magnets. When a quench was detected, the QPM simultaneously energized heaters within each magnet to enlarge the quenched region and enabled switches to bypass current out of the affected magnets. In addition, it initiated a beam abort, to reduce the impact of the orbit distortion caused by the decaying magnetic field of the quenched magnets.

A key component of protecting the silicon detector was the Tevatron QPM being able to detect a quench and abort the beam as early as possible. The early Tevatron QPM operated at 60 Hz, leading to quenches possibly remaining undetected for up to 16 ms ( $>760$  beam revolutions) between QPM measurement cycles. Indeed, this shortcoming was at the heart of an incident in 2003 that caused considerable damage to the Tevatron and to the experimental detectors. When a movable experimental detector (Roman Pot) suddenly moved toward the beam, high beam losses scattered from the device caused a very fast quench of nearby superconducting magnets that likely went undetected for the entire gap between QPM measurement samples. The beams circulated for most of that time with highly distorted orbits that showered the experiments and accelerator components. A stainless steel collimator had a groove bored into its surface over half of its 1.5 m length. A review of the incident led to a higher bandwidth upgrade of the QPM system (to 5 kHz) completed in 2006 which allowed quenches to be detected and beam aborted in  $\sim 500 \mu\text{s}$  (25 beam revolutions).

### 6.1.4. Separator sparks

In the Tevatron, the proton and antiproton beams circulated within a single beam pipe. Electrostatic separators kicked the beams onto distinct helical orbits so that head-on collisions occurred only at the CDF and D0 interaction points. These 26 separators were stainless steel, parallel-plate electrodes, 2.5 m long, with a 5 cm gap operating with a gradient of up to  $\sim 40$  kV/cm. Occasionally, a high-voltage breakdown (spark) occurred between the plates, or between a plate and the surrounding shell. The effects of a separator spark depended on

which separator broke down, and when the spark occurred during a Tevatron cycle. Such breakdowns caused a momentary kick to the beams resulting in orbit distortions that caused beam loss spikes, emittance growth, and a small drop in instantaneous luminosity. The orbit distortion caused by a separator spark could be large enough to drive beam into collimators and cause quenches of nearby superconducting magnets. Improvements in the high voltage conditioning of the separators reduced the overall spark rate compared to early Run II conditions. During the latter years of Tevatron operations, only one or two stores per year terminated prematurely from a separator spark.

### 6.2. Beam monitoring and detector protection

CDF had a slow-reacting (of the order of seconds) software monitor and a fast-reacting (of the order of  $10\ \mu\text{s}$ ) hardware protection system to help prevent damage to the silicon detector from the incidents mentioned in Section 6.1.

The software program, called `TEVMON`, collected several measurements that described beam conditions, some of which were provided to CDF by accelerator monitoring systems. These included beam losses, RF station voltages, instantaneous luminosity, abort-gap beam current, and abort kicker magnet voltages. A variable that entered the warning range caused an audible alert for the shift crew, which indicated degraded beam conditions that may warrant their attention. When `TEVMON` reached the alarm state, the bias voltages of the silicon detector were turned off automatically.

The fast reacting hardware protection systems, the beam condition monitoring (BCM), consisted of four Beam Loss Monitors (BLMs). These were two ionization chambers on the east and two on the west side of the detector, about 4.3 m from the nominal interaction point (IP) and at a radius of about 20 cm from the beam axis. The location of the BLMs from the IP was necessary due to their size, which made it impossible to put them inside the detector. The BLMs were read out every  $210\ \mu\text{s}$  (10 beam revolutions), and a circular buffer of 2048 measurements was kept. The BLMs monitored the radiation accumulated over the last minute and the radiation rate. An accumulated dose greater than 19 rads (0.19 Gy) over the previous minute would issue an *integrated dose alarm*, whereupon the shift crew would pass on the alarm to the Tevatron operators and adjustments to the Tevatron operation would be made. If the radiation rate exceeded 12 rads/s (0.12 Gy/sec), the *radiation abort alarm* would fire, whereupon the Tevatron would automatically issue an abort and the beams would be dumped.

A closer examination of beam incidents showed the BLMs lacked the timing resolution and dynamic range to foresee the conditions leading to an *radiation abort*. A system of smaller sensors, closer to the beam and with a faster read-out system, could abort the beam more rapidly to improve the safety of the CDF silicon detector. This led to the installation of a diamond-based BCM system [40]. A total of thirteen diamond sensors were installed in the CDF detector, at the locations indicated in Fig. 13. Two groups of four diamond-based sensors were located inside the tracking volume, with each group mounted in a support structures at a distance of 1.7 m from the nominal IP, arranged as the

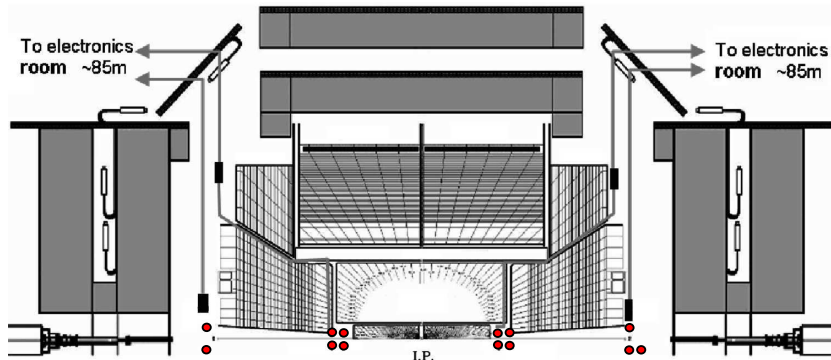


Figure 13: The locations of the diamond-based BCM system in the CDF detector. The picture shows the upper hemisphere of the CDF detector. The proton beam circulated from left-to-right along the horizontal axis, colliding with the anti-proton beam that circulated in the opposite direction. The collision occurred at the interaction point, indicated by “I.P.” in the figure. A pair of four red dots, symmetrically placed on either side of the IP, indicate the sensors inside the tracking volume, and the red dots further away from IP along the beamline indicate sensors outside the tracking volume.

sides of a 4 cm by 4 cm square. Five more diamond-based sensors were installed outside the tracking volume, on the previous BLM system support structure; two diamonds on the west side and three on the east side.

The BCM system was configured to abort the Tevatron beams when at least four diamond sensors measured a current of at least 500 nA and the CDF solenoid was fully energized, as the diamond dark current was affected by the external magnetic field. These settings were determined from a six-month study period to optimize the thresholds, and allowed quick response to potential beam incidents, while minimizing the number of false aborts. In general, the response of the diamonds was found to be significantly faster than that of the BLM-based devices.

## 7. Sensor readout calibration

The algorithm that forms clusters from individual hits in the silicon detector uses the measured pedestal mean and RMS values for each individual strip to separate actual signals from noise fluctuations. These values were measured bi-weekly for each channel during Run II with special calibration runs and recorded in the experiment database. A standard silicon calibration required two runs taken in read-all mode: one with DPS turned off and one with DPS turned on.

The analysis of data from these runs started with accumulation of the ADC pulse height distributions for individual channels. Section 3.3.1 describes the DPS circuitry, in particular that the start of the ADC counter is delayed until a fraction  $f_d$  of the 128 channels in the chip have a voltage below a common voltage ramp. This fraction  $f_d$  can vary from chip to chip but is close to 33/128 channels. A comparator switches state when the fraction of channels exceeds  $f_d$ , and a

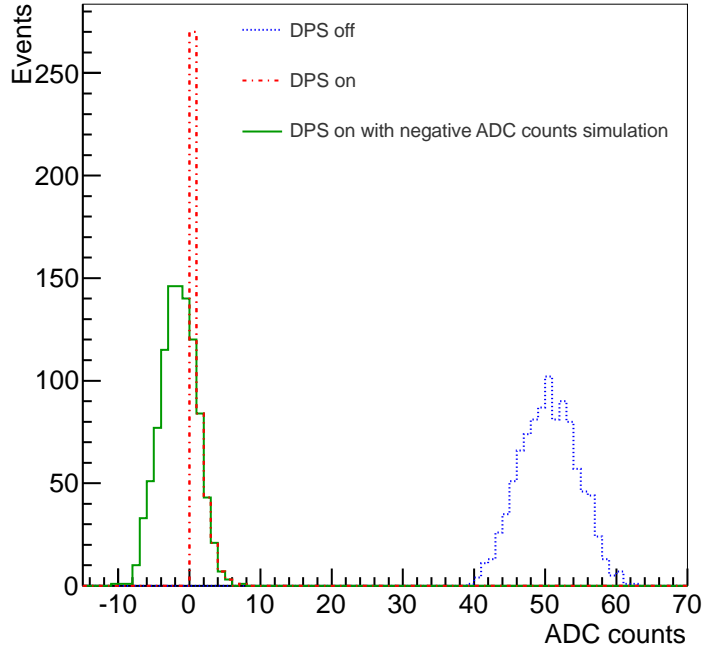


Figure 14: Effect of Dynamic Pedestal Subtraction on pulse height distribution of a single channel in 1000 events. The DPS-off distribution is shown as dotted blue, DPS-on as dot-dashed red, and the solid green histogram is an extrapolation of what the DPS-on distribution would be if negative ADC counts could be recorded. The peak at 0 ADC counts in the DPS-on distribution is suppressed by choice of scale.

finite propagation delay  $t_d$  exists between the time the comparator switches state and the start of the ADC counter. Because of the delay, the effective pedestal values in this scheme are negative for most of the channels and the distribution from DPS-on data is not sufficient to determine the pedestal mean and RMS. Instead, the expected DPS-on distribution is calculated from the measured DPS-off distribution with a simulation of the DPS algorithm that uses the values of  $t_d$  determined for each chip during commissioning. The effect of the DPS circuit on the pulse height distribution of a single channel is illustrated in Fig. 14, in which the value of  $t_d$  is exaggerated for illustration purposes.

The pedestal and noise values for each individual channel were stored in the offline calibration database. Channels were flagged as *dead* or *noisy* based on their expected occupancy. Noisy channels are not included in the default offline clustering algorithm. The calibration constants stored in the offline database are used for data reconstruction as well as detector simulation.



## 8. Detector monitoring and operations support

The operation and maintenance of the silicon detectors required dedicated personnel and software for fast problem response. The CDF Silicon Group was comprised of approximately ten on-call experts who provided 24-hour support to the CDF operations group and performed regular maintenance to ensure optimal performance of the detector. The group was led by two sub-project leaders. Two experts were assigned to each of the following subsystems: DAQ, power supplies, and cooling. Another expert periodically performed calibrations of the detectors and ensured their quality. In addition, three to four experts provided online monitoring of the detector and gave prompt feedback to the group of any developing hardware problems. The group strived to optimize and automate most aspects of the silicon detector operations over the years.

Many software packages were developed for detector operations and monitoring. They were broadly divided into three categories: stand-alone java applications used by the shift crew, scheduled jobs to acquire data on power supplies and the cooling and DAQ systems, and Perl-based CGI scripts that provided real-time information to the Silicon Group.

### 8.1. *Silicon auto-recovery*

The SVX3D readout chips (see Section 3.3.1) required proper initialization sequence as soon as they were powered. The process of turning on power to the silicon detectors required synchronized actions in both the power supply control and the DAQ. Over time, a set of well established procedures to recover from common failure modes was developed. However these manual recovery procedures reduced the data-taking efficiency, especially when a large fraction of the detector channels needed to be turned on after failures, such as a power supply crate reset (see Section 4.3).

In order to automate and speed up the recovery of power to the detector channels, a *Silicon Auto-Recovery* (SAR) software tool was developed. SAR detected channels that lost power during data-taking and sent a request to the power supply control to turn these channels back on. Once the power to the chips was restored, SAR took the corresponding FIB through the initialization process which also initialized the chips. During this process, data taking was suspended. After automating both the power supply crate reset and recovery, the average experimental downtime due to lost communication (see Section 4.3) with the power supply crates was reduced from 10 min down to less than 5 min.

### 8.2. *SVXMon*

*SVXMon* was the monitoring application used for both online and offline diagnostics of the CDF silicon detector problems. It ran continuously during data taking as part of a set of CDF monitoring applications. It accumulated various statistics and presented a coherent set of silicon performance plots to the shift crew. On special occasions, it sent automated requests to reinitialize DAQ components showing problems.

SVXMon was a highly configurable program capable of presenting both very general and very detailed views of the silicon data. For each silicon strip, SVXMon accumulated the number of hits and pulse height distribution. These were used to create plots of occupancies, average pulse heights, distribution shapes, etc., with various degrees of detector granularity. The monitoring application had a large number of configuration parameters which evolved over time to optimize the information useful to detect and understand error conditions in the silicon detectors.

### 8.3. *IMON*

*IMON* was an application used to monitor currents in the silicon detectors. *IMON* displayed each ladder of the detector as a set of color-coded boxes (one for each channel of the ladder). If the measured current was within a pre-set range, then the box showed up green. If it was just outside the good range, it showed up yellow. If it was far outside that range, it turned pink<sup>4</sup>. When a ladder turned pink, it alerted the shift crew so they could take action.

As the sensors degraded due to exposure to radiation, they drew more current. Eventually, a sensor drew enough current to send it over the pre-defined “good” range; this was normal and simply required adjustment of the good range for that particular sensor by a member of the Silicon Group. A typical bias channel drew an additional 30  $\mu\text{A}$  of current for every 500  $\text{pb}^{-1}$  of delivered integrated luminosity. The currents drawn by the chip chains did not change. When one exceeded the normal limits, it typically needed to be reinitialized.

Although the concept for adjusting the bias current limits was simple, the actual procedure was tedious. Limits for the bias currents were adjusted and documented in a database. The rate of increase varied widely across the channels due to the sensor type, radiation exposure, and other causes. With close to 500 bias channels, 25–50 adjustments were made every week. Changing the limits by hand could take several minutes per channel. For bias channels which had increases consistent with normal aging, the limits were adjusted by a monitoring program. After automatic adjustment software was made operational, it took care of approximately 95% of the limit adjustments, drastically cutting down the workload of the Silicon Group.

### 8.4. *ADCMon*

The Silicon Group had the responsibility to ensure good quality of the data collected by the silicon detectors. *ADCMon* was an application developed to ease that task. *ADCMon* read the raw information recorded by the DAQ and provided the distributions of charge in ADC counts for each silicon ladder. Two different versions of *ADCMon* were implemented: online and offline. The online version operated in the CDF control room during data taking and provided data to SVXMon. It provided the charge distribution of the last 500 events, as well

---

<sup>4</sup>Other colors were used to indicate ladders which had tripped, turned off, had lost communication or were ignored by the DAQ.

as the statistics accumulated during the entire run of data taking. The offline version was executed with a delay of less than one day from the end of the run and was useful to understand long term behavior of the silicon ladders. It generated a table of histograms representing the charge distribution for events of a given run in comparison with a reference run. It also provided information about the percentage of bit errors in digital transmission of data.

Optical data transmission bits could permanently get stuck in a high or low state due to radiation damage, cable or electronics malfunction, as described in Section 3.8.2. This could lead to a lower resolution of the charge distribution. Discrepancies in the shape of charge distributions or absence of data could be caused by a FIB or power supply failure. Severely underdepleted ladders could show an observable drop in the high end of the charge distributions. A visual evaluation of the offline results required 5–10 min per day.

### 8.5. *iFIX*

Some components of the silicon detector needed to be monitored independent of data taking. A system to do this was developed based on the commercial automation software *Proficy HMI/SCADA iFIX*, licensed by GE Fanuc [41]. Data were stored at intervals on the order of a few seconds, with recent readings ranging from a few hours to a few days being displayed in the CDF control room. Older data were migrated to permanent storage. This information could be retrieved from iFIX computer nodes.

#### 8.5.1. *Slow control of cooling system*

An iFIX node was connected to the PLC system through a VME module to a Siemens SIMATIC 505 Crate, where the I/O modules resided (see Fig. 12 in Section 5.2). Information from the cooling related devices was available in the iFIX software which provided displays of real-time readings of the devices (temperature sensors, pressure gauges, flowmeters, valves, etc). Changes to parameters of selected devices could be made through this system. The system-wide and sub-component interlock status were also displayed. In particular, the most valuable quantities monitored in this system were the temperatures of the cooling lines inside the detector, as well as the flows and pressures.

#### 8.5.2. *Audible alarm system*

Alarm conditions were defined for selected variables, such as the cooling variables which could potentially trigger the interlocks. In the case of temperatures, pressures and flows, low and high warning and alarm limits were defined. Other variables in the alarm list included the high voltage and trip status of power supplies. Any alarm going off was followed by an audible voice alarm.

#### 8.5.3. *Monitoring of rack modules*

The status of the AC power to the racks hosting the FIB and CAEN crates in the collision hall was monitored, and remote power cycling of racks was possible. In addition, monitoring and alarming on low-voltage status was available for

small devices in the racks, such as fans inside the crates. This was also true for the racks hosting the VRB modules outside the collision hall. We also monitored the power supply output voltages for the VRB and FIB crates.

#### 8.5.4. Reset of silicon power supplies

The automatic reset of CAEN power supply crates (explained in Section 4.3) was monitored in the iFIX system. Additionally, the silicon operations team could manually reset any power supply crate from this system.

## 9. Monitoring radiation damage effects

### 9.1. Depletion voltages

Periodically, the depletion voltage of each sensor was measured to monitor the radiation effects on the sensor, and the operating voltage increased to ensure that the sensors remained fully depleted. The operational definition of depletion voltage for the CDF silicon detectors was the bias voltage at which the charge collection saturates. Specifically, the voltage at which the charge collected was 95% of the maximum value. Operating at bias voltages larger than a depletion voltage defined this way ensured the best detector performance.

Two different methods to measure the depletion voltage were used: the *noise scan* was used for double-sided sensors that had not undergone type inversion, and the *signal scan* was used for all sensors. In each case, the bias voltage was changed and either the signal from charged tracks or the noise in the sensor was measured. The results of both methods are presented here in the context of operating the detector. Further discussion of the observed effects of radiation damage in the sensors is reserved for a future article dedicated to this topic.

#### 9.1.1. Noise scans

The noise scan measured the average noise for each ladder as a function of bias voltage. For each bias voltage setting, data were taken in read-all mode and the ADC count distribution for each strip was recorded. For each ladder, the noise was determined by taking the RMS of the ADC distribution for each strip and then averaged over the strips on the p-side ( $r-\phi$ ) and the n-side ( $r-z$ ) separately.

The depletion voltage for each ladder was determined by fitting the n-side noise as a function of the bias voltage to a sigmoid function

$$\text{noise} = A + \frac{B}{1 + \exp[-C(V - D)]} \quad (1)$$

where  $A, B, C$  and  $D$  are fit parameters and the variable  $V$  is the bias voltage. The depletion voltage was identified as the voltage at which the function is equal to the sum of lower plateau of the sigmoid function and 5% of the height of the fitted sigmoid function, or  $V_{dep} = D(\ln 19)/C$ .

Noise scans for a typical ladder taken at different integrated luminosities are shown in Fig. 15. In the early scans, the separation between the two noise levels

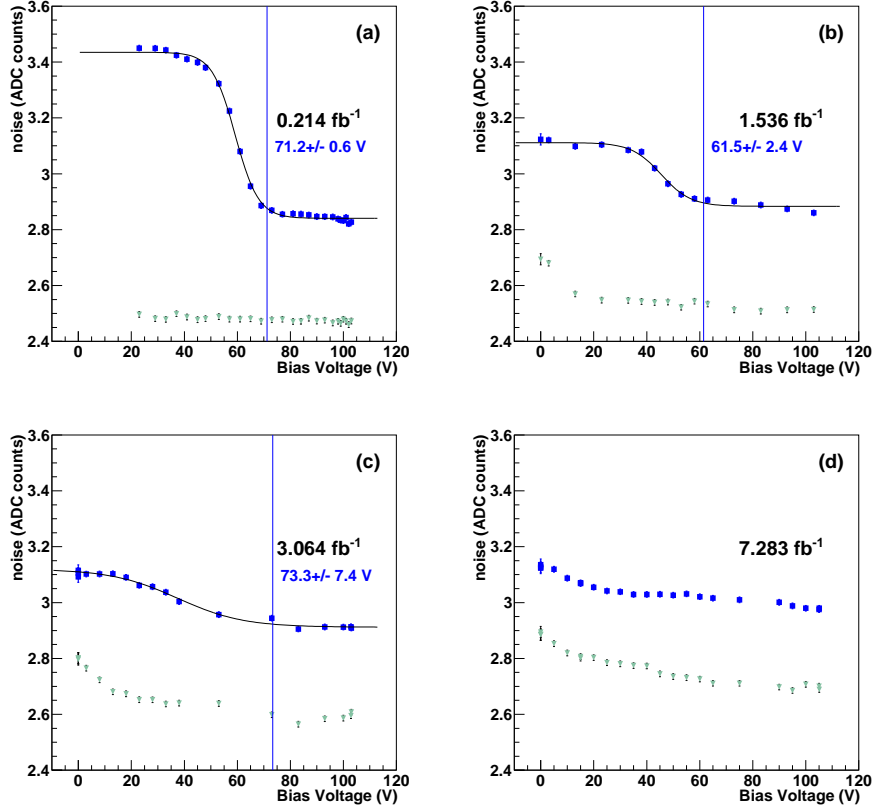


Figure 15: Noise scan measurements for a single ladder from layer 1 of SVX-II at four different integrated luminosities (given in  $\text{fb}^{-1}$ ). The blue squares are the measured noise on the n-side. The pale green triangles are the measured noise on the p-side of the sensor. The extracted depletion voltage is indicated with a vertical line.

for the n-side was large, and the depletion voltage was easily determined, as seen from Fig. 15(a). As the sensor became irradiated, the underdepleted noise level decreased while the depleted noise level increased, and it became increasingly difficult to determine the depletion voltage using this method. Specifically, noise scans where the two noise levels of the n-side were separated by less than 0.2 ADC counts did not give a reliable determination of the depletion voltage. Fig. 15(d) shows the measured noise after inversion of the sensor, for which the p-side noise and n-side noise have similar behavior. After the inversion, the overall noise level increased with radiation dose as expected, but the shape of the curves remained the same.

The noise scan method was used to monitor the depletion voltage before the inversion of the sensors. Fig. 16 shows the average depletion voltage for ladders in layers 0,1, and 3. Noise scans where the two noise levels of the n-side

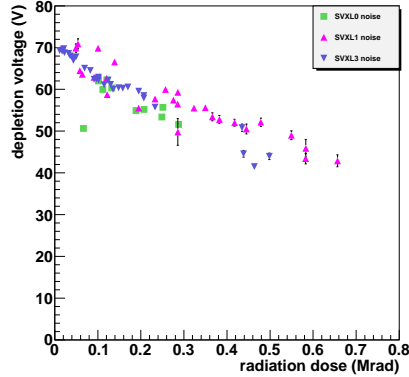


Figure 16: The average depletion voltage determined from noise scans is plotted for the Hamamatsu sensors in SVX-II (see Table 1) as a function of radiation dose.

Layer	r (cm)	dose/L (kRad/fb <sup>-1</sup> )
L00 narrow	1.35	994 ± 199
L00 wide	1.62	756 ± 151
SVX-L0	2.54	385 ± 77
SVX-L1	4.12	186 ± 37
SVX-L2	6.52	94 ± 19
SVX-L3	8.22	66 ± 13
SVX-L4	10.10	49 ± 10

Table 2: The radiation dose per unit luminosity measured by the TLDs in the CDF tracking volume [42], extrapolated to the location of the individual silicon layers .

were separated by less than 0.2 ADC counts are not included in the plot. In order to compare the different layers, integrated luminosity was converted to the equivalent dose of the radiation field measured inside the CDF detector with over 1000 thermal luminescent dosimeters in 2001 [42], summarized in Table 2. The behavior of the three different layers was remarkably consistent considering that the integrated dose received by the layer depends on the distance from the interaction region. The sensors from layers 2 and 4, which are from a different manufacturer than the other layers, were not included in this analysis because they developed complicated noise profiles and the simple data analysis described above did not give reasonable quantitative results and signal scans were used instead to monitor the depletion voltage.

### 9.2. Signal scans

The signal scan provided the best evaluation of the depletion voltage, and in many cases the only one. The charge collected by the sensor increased with increasing bias voltage as the depleted region in the sensor grew, until the sensor

was fully depleted and the charge saturated. The scan had to be performed with colliding beams and required approximately two hours per layer. To minimize the amount of lost physics data, the scans were done when the instantaneous luminosity was low.

Data were acquired with a specific trigger selecting collision events containing at least two tracks. From these events, tracks traversing the silicon layer under study were identified using the COT and remaining silicon layers. If one and only one cluster existed within  $150 \mu\text{m}$  of the location where the extrapolated track crossed a sensor, the total charge of that cluster was recorded in a histogram. A reasonable fit result required at least 1000 tracks per ladder per bias voltage setting, with additional tracks per point needed below 20 V.

The distribution of cluster charges was fit to the convolution of a Landau function and a Gaussian function in the region around the peak. The upper plots of Fig. 17 are examples of this distribution at two different bias voltages. The most probable value of the fitted function was plotted as a function of bias voltage, and these points were fitted to a sigmoid function of the same form as Eq. 1. The measured depletion voltage was the bias voltage at which the function value is 95% of the total charge is collected, or  $V_{dep} = 0.95 * (A + B)$ . An example is shown in Fig. 17(c). Also shown on this plot is the efficiency, defined as the fraction of tracks for which a cluster is found. Due to the limited data samples of these special runs, the track selection was quite loose, and the absolute value of this efficiency does not reflect normal sensor performance during data taking.

The non-zero value of the cluster charge for bias voltages below 10 V is a measure of the effective clustering threshold for that ladder. All L00 strips were read out every event, while for SVX II and ISL, only strips above 9 ADC counts plus the neighboring strip on either side were read out. In the offline reconstruction, clusters were formed from a set of neighboring strips that satisfied one of the following criteria:

- A single strip has pedestal-corrected ADC count larger than 4 times the measured RMS of its pedestal distribution.
- Two neighboring strips each have pedestal-corrected ADC counts larger than 3 times the measured RMS of their respective pedestal distributions.
- Three neighboring strips each have pedestal-corrected ADC counts larger than 2 times the measured RMS of their respective pedestal distributions.

At low bias voltages, very few clusters are above threshold and the cluster threshold algorithm determines the shape of the cluster charge distribution for these few clusters above threshold. The mean of this distribution is thus a monitor of the effective threshold of the offline clustering algorithm. Although the initial rise of the cluster charge is hidden by the clustering threshold, the increasing efficiency indicates increasing mean cluster charge as more and more clusters are found above the threshold. Because the strip noise increased with radiation dose, these clustering thresholds crept upward with integrated luminosity, and the signal scans allowed them to be monitored.

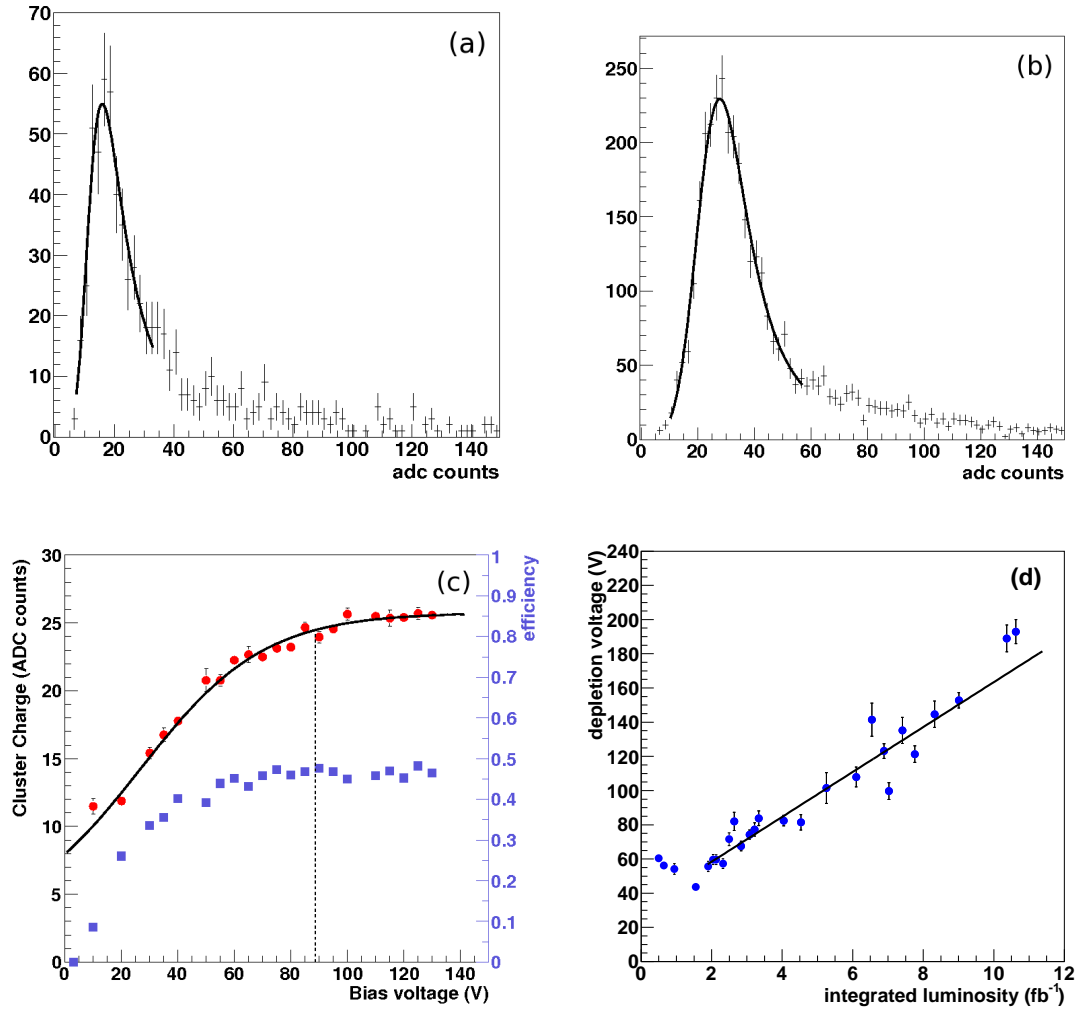


Figure 17: The upper plots show the measured cluster charge distribution for a single L00 ladder at a bias voltage of 30 V (a) and 130 V (b) after  $4 \text{ fb}^{-1}$  of integrated luminosity. Plot (c) shows the peak of the cluster charge distribution (red circles) and the efficiency (blue squares) as a function of bias voltage. The dashed line indicates the depletion voltage extracted from the sigmoid fit. Plot (d) shows the measured depletion voltage for this ladder as a function of integrated luminosity, and the linear fit used to extrapolate to higher luminosity values.



Close monitoring of L00 and the inner layers of SVX was essential after inversion to keep the operating bias voltages above the depletion voltage. Operating voltages were increased on a sensor by sensor basis after extrapolating the linear trend in the measured depletion voltages several months into the future.

Fig. 18 shows the linear fits for the individual L00 ladders as gold or red lines and the average over all the ladders as a black line and blue points. The predicted depletion voltages for all L00 ladders lie well below the power supply limit of 500 V and the sensor breakdown region that starts at 650 V, and they were fully depleted through the end of Run II. Fig. 19 shows the linear fits for the  $r$ - $\phi$  side (p-side) of the first layer of SVX-II (SVX-L0). The fits for individual ladders are shown as red lines and their average as a black line. The blue points are the average measured depletion voltage for all ladders. The power supply limit for these sensors is 250 V and sensor breakdown was expected in the range 170-270 V, indicated with a shaded region.

In agreement with the projections, roughly one third of the SVX-L0 ladders were not fully depleted for an operating voltage of 165 V at the end of Run II. The performance of these underdepleted ladders was only slightly compromised: the charge collected on the p-side was reduced, while the charge collected on the n-side was unaffected. Because of the risk of damage to the sensor, we decided not to operate any ladders above 165 V until the hit efficiency of the ladder began to decrease. Only one ladder reached this condition by the end of the run. That is, the hit efficiency of all but one of the underdepleted ladders was still maximal at the end of the run despite the reduced charge collection on the  $r$ - $\phi$  side (p-side).

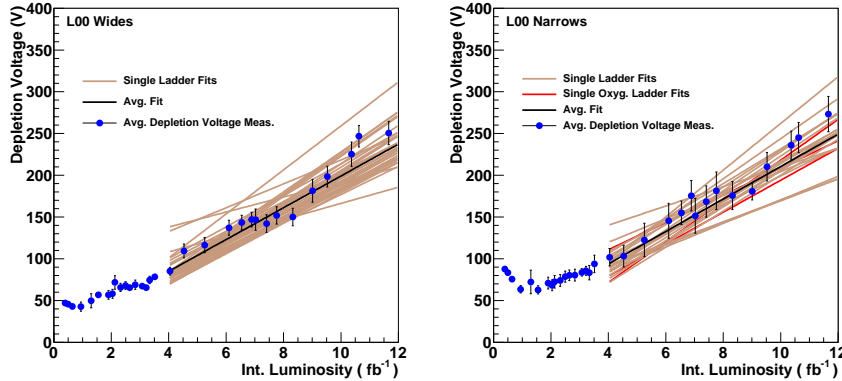


Figure 18: Summary of depletion voltage measurements and fits for L00 wide ladders (left) and narrow ladders (right).

### 9.3. Surprises in the behavior of irradiated sensors

In the traditional model for the electric field in a reverse-biased silicon sensor, the field increases linearly through the bulk when the bias voltage is applied.

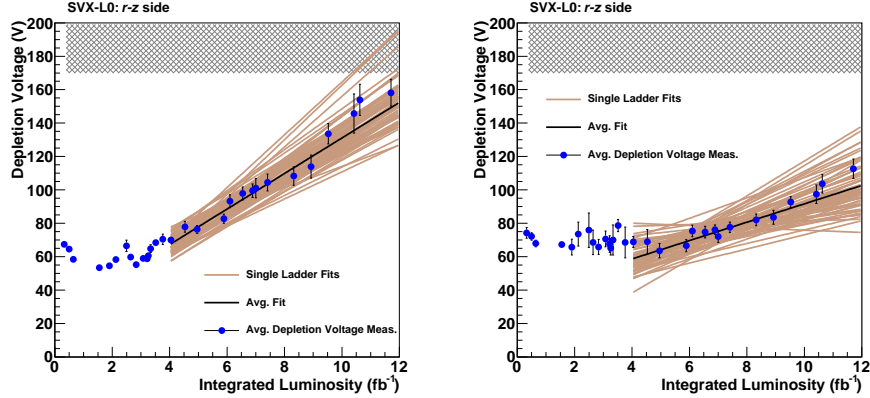


Figure 19: Summary of depletion voltage measurements and fits for the  $r$ - $\phi$  side or p-side (left) and the  $r$ - $z$  side or n-side (right) of SVX-L0 sensors.

There is however evidence that trapped charge in heavily irradiated sensors dramatically affects this simple picture of the field inside the sensor. In CDF, we have observed evidence that, after irradiation, the field was non-uniform and extended from both sides of the sensor. This resulted in a much longer lifetime for SVX-L0 operating with *safe* bias voltages than had been anticipated.

In undamaged CDF sensors, the electric field was highest at the p-side of a reverse biased pn diode junction, and decreased linearly through the bulk material. At bias voltages less than the depletion voltage, the electric field at the n-side was zero and essentially no signal was induced in the n strips as particles passed through the sensor. The general understanding of radiation damage to silicon sensors when the CDF detector was built (summarized in the *Hamburg model* [43]) was that radiation induced crystal damage made the bulk material increasingly more p-type. At sufficiently high dose, the n-type bulk material was expected to become effectively p-type (this is referred to as *type inversion*) and the junction side of the detector was expected to move from the p-side to the n-side. After type inversion, the electric field in the sensor was expected to be highest at the n-side diode junction and to decrease linearly through the bulk material. It was expected that essentially no signal would be recorded on the p-side at bias voltages less than the depletion voltage.

This behavior is now understood to be a consequence of the properties of damaged silicon with an applied bias voltage. In heavily irradiated silicon, the trapping of leakage current charge carriers dramatically affects the electric field inside the sensor. Leakage current is generated approximately uniformly throughout the thickness of the sensor. Electrons carry charge toward the n-side and holes carry charge toward the p-side. This means that the density of moving electrons is highest near the n-side and the density of moving holes is highest near the p-side. Because the equilibrium number of trapped charges depends on the density of moving charges as well as trapping probabilities and

trap lifetimes, the density of trapped electrons is highest near the n-side of the sensor and the density of trapped holes is highest near the p-side of the sensor. These trapped charges create an electric field with maxima at both sides of the sensor. The importance of trapped charges to the static field in heavily irradiated sensors was pointed out by Eremin, Verbitskaya, and Li in 2002 [44]. Swartz *et al.* have tuned a two trap model to fit CMS pixel beam test results, including temperature dependence [45].

The data from the signal scans taken after significant radiation exposure are consistent with an electric field peaking at both faces of the sensor, and clearly inconsistent with the naive expectation of a linearly decreasing field with a single maximum at the n-side. Fig. 20 shows the signal scan data delivered luminosities of  $0.3 \text{ fb}^{-1}$  (above) and  $6.9 \text{ fb}^{-1}$  (below) for a typical sensor in SVX-L0. Because the signal was induced primarily by the motion of charge carriers in the depleted region adjacent to the electrode, the measured cluster charge for a particular voltage was a measure of the size of a possible depleted region adjacent to the electrode. Because of the readout thresholds for the SVX sensors, clusters below 10-15 ADC counts are not detected. However, the fraction of tracks with clusters above this threshold, shown as blue squares in Fig. 20, increased as the average charge collected increased. The upper measurement in Fig. 20 was done when the sensor was only slightly irradiated. The charge collection began at smaller voltages on the p-side than the n-side, compatible with a depleted region that began at the pn junction and grew toward the n-side electrode as the bias voltage increases. The lower measurement was done after  $6.9 \text{ fb}^{-1}$  of luminosity, and the charge collection began at similar bias voltages for each side and increased similarly with increasing voltage. This latter behavior was compatible with an electric field that had two maximums, one at either face of the sensor, creating two depleted regions that started at either face and grew toward the center of the sensor as the bias voltage increased. Similarly, for the p-side of a single sided L00 sensor after  $4 \text{ fb}^{-1}$  of luminosity (post-inversion), Fig. 17(c) shows an early onset and gradual increase of charge collection, again consistent with a doubly peaked electric field.

The unexpected electric field behavior had an important consequence for the longevity of the CDF silicon detector. The SVX-L0 ladders could be operated in a slightly underdepleted state with only a small loss in charge collection and no loss in hit efficiency for a short time after the depletion voltage exceeded the maximum safe operating voltage. Because the *b*-tagging efficiency (Section 10.2) of the detector was insensitive to a small loss in charge collection in a fraction of the SVX-L0 sensors, it was decided to operate these sensors slightly underdepleted instead of risking damage at higher bias voltages.

#### 9.4. Signal-to-noise ratio

During Run II, the signal-to-noise ratio (S/N) of L00 and SVX-II sensors were monitored using well-measured tracks from events selected by the low momentum dimuon trigger. The signal *S* was defined as the summed charge of a cluster of strips associated with a track and corrected for path length. The noise

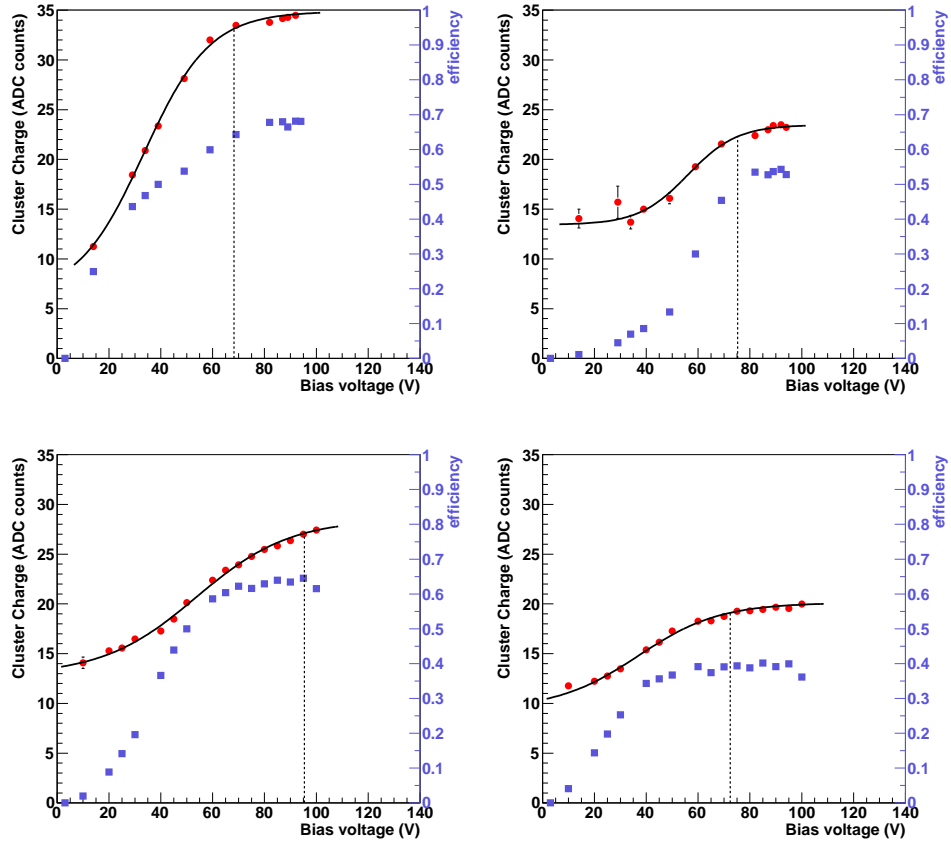


Figure 20: The cluster charge (circles) and efficiency (squares) as a function of bias voltage for the p-side ( $r-\phi$ , left) and n-side ( $r-z$ , right) of a typical SVX-L0 sensor. The dashed line indicates the depletion voltage extracted from the measurement. The upper plots contain data taken after  $0.3 \text{ fb}^{-1}$  of delivered luminosity, the lower plots data taken after  $6.9 \text{ fb}^{-1}$  for a sensor that inverted around  $1.5 \text{ fb}^{-1}$ .

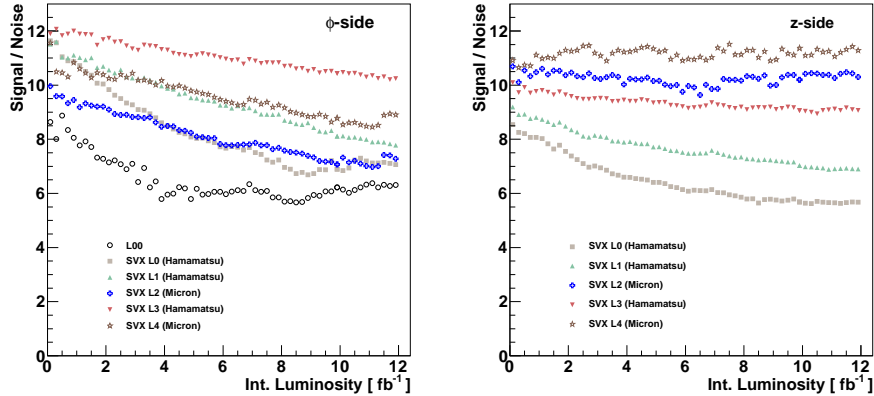


Figure 21: Measured signal-to-noise ratio for L00 (left), the  $r$ - $\phi$  side of SVX-II (left) and the  $r$ - $z$  side of SVX-II (right).

for individual strips was measured during special calibration runs performed bi-weekly with beam, as described in Section 7. The noise of a cluster  $N$  was defined as the average noise of the individual strips belonging to the cluster.

Fig. 21 shows the average measured  $S/N$  ratio for L00 and SVX-II, separately for the  $r$ - $\phi$  and  $r$ - $z$  sides. All ladders that operated consistently well throughout Run II are included, corresponding to roughly 75% of all ladders. As expected, the  $S/N$  ratio decreased more quickly for L00 and SVX-L0 since they were closer to the interaction point and suffered from more radiation damage. The dip in  $S/N$  values for L00 and SVX-L0 near  $8\text{fb}^{-1}$  corresponded to a period of slight underdepletion.

We observed plateaus in the ratios in the L00 and SVX-L0  $S/N$  ratios beginning at  $5\text{fb}^{-1}$  and  $8\text{fb}^{-1}$ , respectively. To verify that the leveling-off was not an artifact of the averaging, the  $S/N$  curves for the individual ladders were investigated. Fig. 22 shows the  $S/N$  trends for the overall L00 average and for three typical ladders whose  $S/N$  values are close to (a) the overall L00 average, (b) the plus-one RMS variation with respect to the overall average, and (c) the minus-one RMS variation with respect to the overall average, where the RMS was defined as the spread of  $S/N$  values for the ladders used in the average. As we observed a plateau-like feature for each ladder, we concluded that it was not due to an averaging artifact. The source of the plateau remains under investigation.

## 10. Physics performance of the silicon detector

Good performance of the silicon detectors was vital to the success of CDF's physics program. In this section we present some of the performance quantities which directly impact the results from analyses requiring silicon tracks or

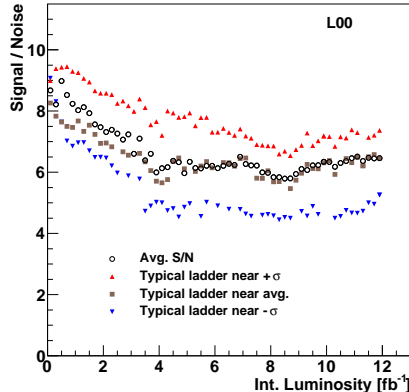


Figure 22: Measured signal-to-noise ratio for the L00 average, and for three ladders that represent typical ladders close to the average, and close to the  $\pm 1$  RMS signal-to-noise values with respect to the average. The RMS represents the spread of signal-to-noise values for the various ladders included in the average.

displaced secondary vertices found by SVT. Reported here are studies on the impact parameter resolution with and without L00, the b-tagging efficiency and the SVT efficiency.

### 10.1. Impact parameter resolution

The impact parameter,  $d_0$  is defined as the shortest distance in the  $r$ - $\phi$  plane between the beam line and the trajectory of the particle obtained from the track fit. The impact parameter resolution  $\sigma_{d_0}$  is a key performance indicator of the CDF silicon detector. This resolution affects identification of long-lived hadrons as well as the ability to study time-dependent phenomena, such as the mixing of  $B_s$  [34] and charm mesons [46]. The detector provided good impact parameter resolution. L00 improved the performance particularly for particles with low momentum or that passed through large amount of passive material [47].

The resolution is parameterized as a function of the particle transverse momentum  $p_T$  as

$$\sigma_{d_0} = \sqrt{A^2 + (B/p_T)^2 + r_{\text{beam}}^2}, \quad (2)$$

where  $A$  is the asymptotic resolution parameter, and  $B$  is the multiple-scattering component. The finite beam size  $r_{\text{beam}} = 32 \mu\text{m}$  accounts for the uncertainty in the location of the primary interaction.

Fig. 23 shows the fitted widths of the cores of the impact parameter distributions for tracks with and without L00 hits as a function of the track  $p_T$ . The inclusion of L00 enhances the impact parameter resolution at low momentum. For tracks that pass through the electrical readout hybrids, the impact parameter resolution is somewhat degraded.

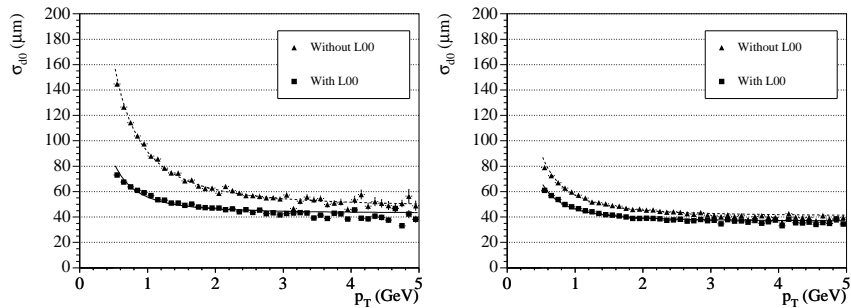


Figure 23: Impact parameter resolutions for tracks as a function of track  $p_T$ . Both plots show the resolutions for tracks before and after the addition of L00 hits. The plot on the left shows the resolutions for tracks that pass through readout hybrids which are mounted on some of the sensors, and the plot on the right shows the performance for tracks that do not pass through hybrids. These plots include the  $r_{\text{beam}}^2$  term in Eq. 2.

Table 3: Fit parameters for the resolutions, shown in the right plot of Fig. 23, for tracks that do not pass through the hybrids. The definitions of the fit parameters are given in Eq. 2. A fixed beam size,  $r_{\text{beam}} = 32 \mu\text{m}$ , is assumed.

Track Category	$A$ ( $\mu\text{m}$ )	$B$ ( $\mu\text{m}$ )
No Hybrid, No L00	$28.6 \pm 0.3$	$35.5 \pm 0.3$
No Hybrid, L00	$17.8 \pm 0.2$	$28.4 \pm 0.1$

Table 3 lists the fit parameters for the tracks with and without L00 hits that do not pass through the hybrids, shown in the right plot of Fig. 23. Tracks used in these fits originate dominantly from interactions in the central region of the detector (in  $z$ ), where using a constant resolution term for the beam envelope is a reasonable approximation. The addition of L00 hits to tracks vastly improves the impact parameter resolution for low momentum tracks and provides a relatively modest improvement of the asymptotic resolution at high momentum. Furthermore, knowledge of the impact parameter is limited by the beam size unless a primary interacting vertex is reconstructed with many high-momentum tracks.

### 10.2. $b$ -Tagging efficiency

Many of the physics goals of the CDF experiment rely on the identification of weakly decaying bottom hadrons. The mean lifetime of these hadrons is approximately 1.5 ps, and the mean decay length is order of a few millimeters. The fact that the weakly decaying hadrons have large boosts means that the particles from the decay travel in approximately the same direction as the parent hadron, with their kinematic distributions depending on the mass of the parent hadron. Precise measurement of the track positions allows tracks originating from displaced vertices to be distinguished from tracks that originate at the primary vertex. Most jets of hadrons produced in  $p\bar{p}$  collisions do not contain bottom or charm hadrons, and very strong rejection of falsely tagged light-flavor

jets is another important figure of merit for the tracker.

CDF uses a displaced-vertex algorithm, SECVTX [48], to identify — or *b-tag* — secondary vertices that are significantly displaced from the beamline. It has two configurations, referred to as “loose” and “tight”, which refer to the track and vertex requirements used to form the displaced-vertex candidates. With the loose requirements, more displaced vertices from heavy hadron decay are identified than the tight requirements, but with a higher rate of falsely tagged light-flavor jets.

The assignment of silicon hits to tracks has a large impact on the efficiency of the algorithm to identify the decays of heavy hadrons, as at least two well-measured tracks are required to form a displaced vertex, and the presence of hits in multiple silicon layers in the inner tracking volume improves the chances of finding that the vertex is significantly displaced from the primary. The tails in the impact parameter resolution — due to hard nuclear collisions with detector material, multiple scattering, and mis-assigned hits in the silicon detector and COT — determine the false tag rate.

The efficiency of the algorithm to identify heavy hadrons increases with the hadron momentum. The efficiency is not measured directly since not all hadron decay products are reconstructed; instead it is parameterized as a function of the transverse energy  $E_T$  of the jet and shown in Fig. 24. The efficiency rises with momentum because the tracks that result from the decay are better measured at higher energy, and the decay flight distance is also longer. At very high  $E_T$ , the tagging efficiency drops, as tracks begin to share hits, with the jets becoming more collimated. Fig. 24 also shows the *b-tag* efficiency as a function of the pseudorapidity,  $|\eta|$ , of the jet. Jets at higher pseudorapidity pass through more material and have fewer COT hits, reducing the tag efficiency and raising the false tag rate as shown in Fig. 25. At very high pseudorapidity, the loss of tracking efficiency in the COT also reduces the false tag rate.

At high instantaneous luminosities, the average occupancy of the silicon detector and the inner layers of the COT rises. This leads to increased chance of assigning noise hits to the tracks as well as missed COT hits due to ambiguity in resolving many overlapping tracks. As a result, at higher instantaneous luminosities, the *b-tag* efficiency drops slightly and the fake tag rate rises. The *b-tag* efficiency is shown in Fig. 26 as a function of the number of reconstructed primary vertices per beam crossing, which is more directly related to the tracking occupancy than the instantaneous luminosity. The *b-tagging* performance is remarkably robust at high luminosities due to the high granularity of the silicon detector covering the low radii tracking region.

### 10.3. SVT efficiency study

Aging of and radiation damage to the silicon detector resulted in increased noise and reduction of the level of the signal (see Section 9.4). These factors degraded the performance and efficiency of the SVT (see Section 3.1.1). A study was performed during the Tevatron run to measure the SVT efficiency as a function of total integrated luminosity and estimate any potential impact on physics analyses. Starting from the measured level of signal and noise in



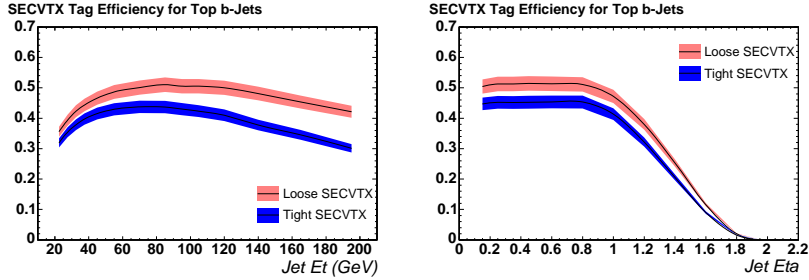


Figure 24: Efficiency of the displaced vertex  $b$ -tagger, as functions of jet  $E_T$  and jet pseudorapidity, for two configurations of the  $b$ -tagger. The efficiency is obtained from tagging jets which have been matched to  $b$  quarks in Monte Carlo top quark decays, multiplied by data/MC scale factors.

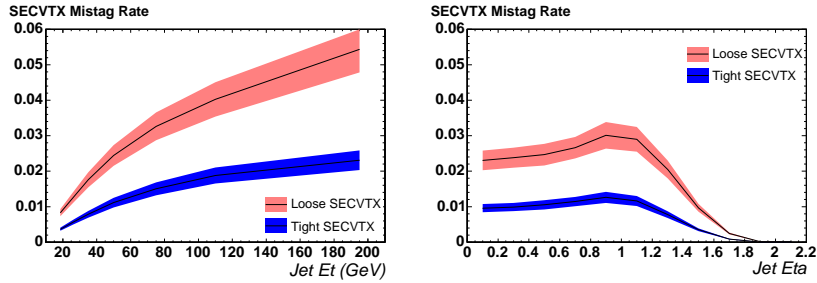


Figure 25: Probability of non- $b$ -jets to be  $b$ -tagged for the displaced vertex  $b$ -tagger, as functions of jet  $E_T$  and jet pseudorapidity, for two configurations of the  $b$ -tagger. The probabilities have been measured from inclusive jet data.

the silicon detector for a reference data sample at  $3 \text{ fb}^{-1}$ , simulated samples were produced by applying extrapolations of the signal and noise up to  $8 \text{ fb}^{-1}$ . Each of the samples was used as input to SVT simulation software to estimate track finding efficiency in  $J/\psi$  events at the corresponding integrated luminosity. Fig. 27 shows the prediction of the SVT efficiency as a function of total integrated luminosity for four (open circles) and all five (closed circles) layers of SVX-II.

A decrease of SVT efficiency of about 4% was predicted between  $3\text{-}8 \text{ fb}^{-1}$ , while the impact of losing an SVX-II layer was about 13%.

## 11. Summary

The CDF silicon detector, consisting of the SVX-II, ISL, and L00 components, was designed to withstand only  $2\text{-}3 \text{ fb}^{-1}$  of integrated  $p\bar{p}$  collision luminosity and was expected to be replaced in 2004 by an upgrade. It ran successfully for over 10 years, through 2011, and was exposed to about  $12 \text{ fb}^{-1}$  of

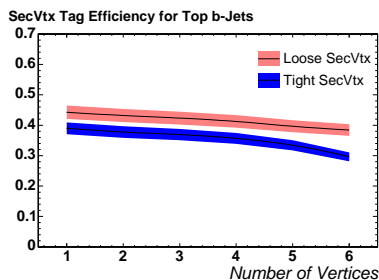


Figure 26: Efficiency of the displaced vertex  $b$ -tagger, as a function of the number of reconstructed  $p\bar{p}$  collision vertices per beam crossing, for two configurations of the  $b$ -tagger. The efficiency is obtained from tagging jets which have been matched to  $b$  quarks in Monte Carlo top quark decays, multiplied by data/MC scale factors.

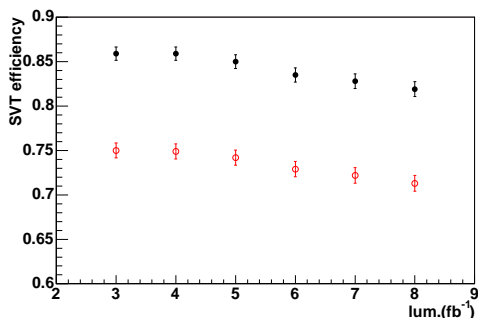


Figure 27: Prediction of the track finding efficiency of SVT as a function of total integrated luminosity. The efficiency is measured in di-muon events from  $J/\psi$  decays. Closed black circles show the efficiency when only four layers of SVX-II are used by the SVT algorithm; empty red circles show the efficiency including all five layers.

integrated luminosity. About 90% of its ladders took data with high efficiency until the end of Tevatron Run II. This was an unprecedented feat compared to any silicon detector in the same category prior to it. It was also the first silicon detector system to be incorporated into a hardware trigger to identify tracks from secondary vertices. It provided precise measurements of the trajectories of charged particles which were important to identify and measure heavy-flavored hadrons, which in turn were crucial to CDF's physics program, including top quark,  $b$  hadron, and Higgs boson physics.

The detector consisted of about 722,000 readout channels, with approximately 500 independent ladders, which required voltages to bias the sensors as well as run the data acquisition electronics mounted on the detector. Elaborate data acquisition, trigger, cooling, and monitoring systems were required to collect the data used for analysis. The detector itself was located inside the drift chamber in a volume heavily congested with cabling, cooling pipes, and the

beam pipe, that rendered it largely inaccessible for repair. Due to its inherent complexity, the detector operations involved detailed procedures and required specially trained experts to execute them. Keeping up with the loss of experts and training new ones to replace them was one of the major challenges faced by the silicon operations team. In addition, inaccessibility of the detector required that every detector access be planned elaborately and well in advance to take advantage of the Tevatron shutdowns. Future experiments must take extra care in designing the accessibility aspects of their subsystems to avoid these situations.

The silicon detector system had its share of failure modes, most of which were addressed during commissioning and the rest were mitigated during the operation of the detector. The most serious failure modes, those that required immediate response, such as power supply failures, cooling system failures, and unsafe beam conditions, had dedicated hardware and software systems designed to protect the silicon detector from damage.

Unanticipated failure modes and exposures to detector damage became evident as Run II of the Tevatron progressed. These had been addressed with hardware modifications, monitoring, review, and improved operational procedures to reduce the chance of damage to the detector. For example, the Lorentz force on bond wires perpendicular to the magnetic field, connecting one side of a ladder to another, on rare instances caused the wires to vibrate at their mechanical resonant frequency and eventually break (Section 3.6). A hardware device was devised and installed to stop data acquisition when the trigger system requested readouts at high frequencies and at regular intervals. Another issue involved spontaneous energizing of the kicker magnets or separators sparking at unexpected times, which steer the beams near the silicon detector and caused damage to it due to the acute radiation dose (Section 6.1.2). The addition of a collimator near CDF and improvement to the high voltage conditioning of the separators had minimized the effect of such incidents on the silicon detector. Careful monitoring of beam conditions, automatic ramp-down of the bias voltage in case of bad beam conditions and beam abort requests from the diamond sensors had also protected the silicon detector from damage due to beam incidents.

Certain electronic components necessary for the functioning of the silicon detector were located in the collision hall. Radiation caused temporary and permanent failures of data acquisition electronics, particularly FPGAs (Section 3.8.1). The power supplies were also susceptible to radiation-induced failures (Section 4.3). Many of the temporary failures could be addressed simply by resetting and re-initializing the affected components, and these procedures were highly automated so that the reset and recovery to the nominal data-taking configuration resulted in a minimum of downtime. Permanent failures of collision hall electronics typically required short accesses to replace the affected components. A sufficiently large pool of spares was kept on hand to maintain a high availability of the detector. Many of the components were repaired at Fermilab, and others required sending equipment back to the manufacturer.

The cooling system for SVX-II and L00 worked remarkably well, while that

of ISL experienced higher failure rates (Section 5). The initial epoxy blockages were cleared with laser light guided inside the small cooling tubes with fiber optics. A later incident stemming from acidified ISL coolant caused leaks in the piping cooling the portcards. These leaks were sealed with epoxy from inside the pipes as the outside was inaccessible. The ISL coolant was returned to distilled water, as in early running phase, and care was taken to monitor and respond rapidly to changes in the cooling system. Nonetheless, as the system aged, leaks in the piping became larger. These did not impact the operation as the coolant ran below atmospheric pressure.

The unexpectedly high longevity of the silicon detector, which came as a welcome surprise, is in part due to the slow aging of the sensors as radiation dose was accumulated (Section 9). The inner layers of the detector type-inverted as expected. The depletion voltage, signal response and noise behaved as expected also after type inversion. There was evidence that the electric field was not a linear function of the position within the sensor, but instead strengthened near the p+ and n+ implants. This created two depletion regions, one on either side of an underdepleted bulk. Sensors that were not fully depleted at the end of Run-II still provided usable data on both sides of the sensor, with slightly reduced charge collection on the p-side.

As a result of its size and complexity, the CDF silicon detector required a dedicated team of experts to operate and maintain it, ensuring the continuous harvest of high quality data. Despite the challenges from a prolonged run and the gradual reduction of spares and experts toward the end of Run II, the data taking was concluded successfully due to extensive efforts on procedure automation and diligent monitoring of every subsystem. Sufficient experience with detector aging, operational failure modes and their mitigation gained along the way ensured good performance during the final years of Tevatron running at high luminosity. Many profound successes of the CDF physics program were the direct result of the high quality data provided by the silicon detector and the dedicated displaced vertex triggers based on it.

## 12. Acknowledgements

The authors would like to thank Dr. D. Christian and Dr. T. Zimmerman of Fermilab for useful discussions on radiation damage in silicon detectors and SVX3D chip functionalities, respectively. This work would not have been possible without a strong support by the CDF operations management and the spokespersons. We also thank the Fermilab staff and the technical staffs of the participating institutions for their vital contributions. This work was supported by the U.S. Department of Energy and National Science Foundation; the Italian Istituto Nazionale di Fisica Nucleare; the Ministry of Education, Culture, Sports, Science and Technology of Japan; the Natural Sciences and Engineering Research Council of Canada; the National Science Council of the Republic of China; the Swiss National Science Foundation; the A.P. Sloan Foundation; the Bundesministerium für Bildung und Forschung, Germany; the Korean World

Class University Program, the National Research Foundation of Korea; the Science and Technology Facilities Council and the Royal Society, UK; the Russian Foundation for Basic Research; the Ministerio de Ciencia e Innovación, and Programa Consolider-Ingenio 2010, Spain; the Slovak R&D Agency; the Academy of Finland; and the Australian Research Council (ARC).

## References

- [1] CDF Collaboration, The CDF II Detector Technical Design Report, FERMILAB-Pub-96/390-E (1996).
- [2] K. Anikeev *et al.*, B Physics at the Tevatron: Run II and Beyond, hep-ph/0201071v2 (2002).
- [3] TEVNPH (Tevatron New Phenomena and Higgs Working Group), CDF Collaboration, D0 Collaboration, Combined CDF and D0 search for standard model Higgs Boson production with up to 10.0  $fb^{-1}$  of Data, FERMILAB-CONF-12-065-E, CDF-NOTE-10806, D0-NOTE-6303 (2012).
- [4] D. A. Toback, AIP Conference Proceedings **753** (2005) 373–382.
- [5] P. Azzi, AIP Conference Proceedings **794** (2005) 66–69.
- [6] T. Akimoto *et al.*, Nuclear Instruments and Methods in Physics Research Section A **556** (2006) 459 – 481.
- [7] A. W. Jung *et al.*, Physics Procedia **37** (2012) 1003–1008.
- [8] M. Weber, Operational experience with the D0 silicon tracker, PoS VERTEX2008 (2008) 001.
- [9] S. Desai, Radiation Damage Study of the D0 Silicon Microstrip Tracker, PoS VERTEX2008 (2008) 013.
- [10] P. Merkel, Nuclear Instruments and Methods in Physics Research Section A **501** (1) (2003) 1 – 6, Proceedings of the 10th International Workshop on Vertex Detectors.
- [11] C. S. Hill, Nuclear Instruments and Methods in Physics Research Section A **511** (1-2) (2003) 118 – 120, Proceedings of the 11th International Workshop on Vertex Detectors.
- [12] S. Hou, Nuclear Instruments and Methods in Physics Research Section A **511** (1-2) (2003) 166 – 170, Proceedings of the 11th International Workshop on Vertex Detectors.
- [13] G. Bolla *et al.*, Nuclear Instruments and Methods in Physics Research Section A **518** (1-2) (2004) 277 – 280, Frontier Detectors for Frontier Physics: Proceedings.

- [14] L. Miller, Nuclear Instruments and Methods in Physics Research Section A **518** (1-2) (2004) 281 – 285, Frontier Detectors for Frontier Physics: Proceedings.
- [15] C. S. Hill, Nuclear Instruments and Methods in Physics Research Section A **530** (1-2) (2004) 1 – 6, Proceedings of the 6th International Conference on Large Scale Applications and Radiation Hardness of Semiconductor Detectors.
- [16] T. Nelson, International Journal of Modern Physics A **16S1C** (2001) 1091–1093.
- [17] CDF Collaboration, SVXII simulation and upgrade proposal, CDF/DOC/SEC\_VTX/CDFR/1922 (1992).
- [18] CDF Collaboration, The CDF upgrade, CDF/DOC/CDF/PUBLIC/3171 (1995).
- [19] A. Affolder *et al.*, Nuclear Instruments and Methods in Physics Research Section A **461** (1-3) (2001) 216 – 218, 8th Pisa Meeting on Advanced Detectors.
- [20] Evonik Industries, Rohacell.  
URL <http://www.rohacell.com>
- [21] S. Holmes, R. S. Moore, V. Shiltsev, Journal of Instrumentation **6** (2011) T08001.
- [22] E. J. Thomson *et al.*, IEEE Transactions on Nuclear Science **49** (3) (2002) 1063 – 1070.
- [23] S. Belforte *et al.*, Silicon Vertex Tracker Technical Design Report, CDF/DOC/TRIGGER/PUBLIC/3108 (April 1995).
- [24] B. Ashmanskas *et al.*, Nuclear Instruments and Methods in Physics Research Section A **518** (1-2) (2004) 532 – 536, Frontier Detectors for Frontier Physics: Proceeding.
- [25] J. Adelman *et al.*, Nuclear Instruments and Methods in Physics Research Section A **572** (1) (2007) 361 – 364, Frontier Detectors for Frontier Physics, Proceedings of the 10th Pisa Meeting on Advanced Detectors.
- [26] T. Zimmerman *et al.*, Nuclear Instruments and Methods in Physics Research Section A **409** (1-3) (1998) 369 – 374.
- [27] M. Garcia-Sciveres *et al.*, Nuclear Instruments and Methods in Physics Research Section A **435** (1-2) (1999) 58 – 64.
- [28] D. Sjoegren *et al.*, Radiation effects on the SVX3 chip, CDF/DOC/SEC\_VTX/PUBLIC/4461 (January 1998).

- [29] J. Andresen *et al.*, Radiation hardness of the compact port card for the CDF silicon tracking detector upgrade, CDF/PUB/PRODUCTION/PUBLIC/5535 (January 2001).
- [30] M.L. Chu *et al.*, Nuclear Instruments and Methods in Physics Research Section A **541** (1-2) (2005) 208 – 212, Development and Application of Semiconductor Tracking Detectors: Proceedings of the 5th International Symposium on Development and Application of Semiconductor Tracking Detectors (STD 5).
- [31] VME International Trade Association, VME Standard.  
URL <http://www.vita.com/>
- [32] Chu-Sun Yen *et al.*, Hewlett Packard Journal **43** (5) (1992) 103–115.
- [33] S. Nahn, M. Stanitzki, T. Maruyama, Silicon resonance detection using the Ghostbuster board, CDF/DOC/CDF/PUBLIC/7749 (August 2005).
- [34] A. Abulencia *et al.*, Physical Review Letters **97** (2006) 062003.
- [35] R.J. Tesarek *et al.*, Radiation effects in CDF switching power supplies, CDF/DOC/CDF/PUBLIC/5903 (March 2002).
- [36] Siemens AG, Siemens 575 PLC.  
URL <http://support.automation.siemens.com/>
- [37] Siemens AG, Siemens Quadlog PLC.  
URL <https://eb.automation.siemens.com/>
- [38] G. E. Totten, D. S. Mackenzie (Eds.), Alloy Production and Materials Manufacturing, Vol. 2 of Handbook of Aluminium, CRC Press, Boca Raton, Florida, 2003.
- [39] 3M, Scotch DP190 Epoxy Adhesive.  
URL <http://www.3m.com/>
- [40] P. Dong *et al.*, IEEE Transactions on Nuclear Science **55** (1) (2008) 328–332.
- [41] GE Fanuc, GE Intelligent Platforms.  
URL <http://www.ge-ip.com/products/3311/>
- [42] R.J. Tesarek *et al.*, Nuclear Instruments and Methods in Physics Research Section A **514** (1-3) (2003) 188 – 193, Proceedings of the 4th International Conference on Radiation Effects on Semiconductor Materials, Detectors and Devices.
- [43] M. Moll, Radiation damage in silicon particle detectors: microscopic defects and macroscopic properties, DESY-THESIS-1999-040 (1999).

- [44] V. Eremin, E. Verbitskaya, Z. Li, Nuclear Instruments and Methods in Physics Research Section A **476** (2002) 556 – 564.
- [45] M. Swartz *et al.*, Nuclear Instruments and Methods in Physics Research Section A **565** (1) (2006) 212 – 220, PIXEL 2005: International Workshop on Semiconductor Pixel Detectors for Particles and Imaging.
- [46] T. Aaltonen *et al.*, Physical Review Letters **100** (2008) 121802.
- [47] B. Brau, Nuclear Instruments and Methods in Physics Research Section A **541** (1-2) (2005) 73 – 77, Proceedings of the 5th International Symposium on Development and Application of Semiconductor Tracking Detectors (STD 5).
- [48] D. Acosta *et al.*, Physical Review D **71** (2005) 052003.